# LABORATORY EVALUATIONS ON THE MECHANICAL IMPACT OF NANOPARTICLE ADDITIVES IN A HEAVY WELLBORE CEMENT

By

MARK COLTEN RITCHIE

Bachelor of Science in Mechanical Engineering

Oklahoma State University

Stillwater, OK

2018

Submitted to the Faculty of the
Graduate College of the
Oklahoma State University
in partial fulfillment of
the requirements for
the Degree of
MASTER OF SCIENCE
December 2019

LABORATORY EVALUATIONS ON THE

MECHANICAL IMPACT OF NANOPARTICLE

ADDITIVES IN A HEAVY WELLBORE CEMENT

Thesis Approved:

Dr. Geir Hareland

Thesis Advisor

Dr. Mileva Radonjic

Dr. Runar Nygaard

# ACKNOWLEDGEMENTS

I would like to start by thanking my advisor, Dr. Geir Hareland, for giving me the opportunity to work on this project and providing guidance on the thesis, it became. I would also like to thank my fellow graduate students for providing a helping hand with the lab work. Lastly, I would like to thank Chad Kucko and Matthew Sanders from Petra Machine; as well as the team in the shop at Wheel Dock for helping fabricate the apparatuses used in this study. Without their help, I would not have been able to match the quality of work presented in this thesis.

Acknowledgements reflect the views of the author and are not endorsed by committee members or Oklahoma State University.

Name: Mark Colten Ritchie

Date of Degree: December, 2019

Title of Study: LABORATORY EVALUATIONS ON THE MECHANICAL IMPACT OF NANOPARTICLE ADDITIVES IN A HEAVY WELLBORE CEMENT

Major Field: Petroleum Engineering

Abstract: Ever since its inception, the oil and gas industry has taken a short term approach to maintaining zonal isolation and permeant plugging using wellbore cements. Continuous changes to their environment over the life of a well plague the cement with shifting pressures and temperatures that exploit its brittle nature, as well as its weak bond with steel casing. As a result, failure occurs and allows communication between previously isolated formations. Concern over migratory fluids along the wellbore has given rise to a fresh desire to perfect wellbore and P&A cements by making use of nanoparticle additives. The purpose of this study and the thesis it frames is to evaluate the mechanical impact small concentrations of nanoparticle barite and magnetite have on a heavy wellbore cement. Compressive and tensile strengths of the cement body have been determined and experimental apparatuses and procedures have been established and used to evaluate the bond strength of cement to a steel substrate from both pure tensile as well as shear loadings. Results show that while a significant improvement to the bond strength is seen as the nanoparticle concentration increases, the compressive strength is only marginally improved and a negative impact is seen in the tensile strength of the cement body. Additionally, an increase in stiffness was seen as nanoparticle concentrations increased; and their interactions in a fully hydrated cement were visually observed using scanning electron microscopy (SEM).

TABLE OF CONTENTS

Chapter Page

# LIST OF TABLES

Table Page

# LIST OF FIGURES

Figure Page

# LIST OF EQUATIONS

Equation Page

# NOMENCLATURE

| Symbol | Description |
|---|---|
| A | Area, $in^2$ |
| BWOC | By Weight of Cement, % |
| CH | Calcium-Hydroxide |
| C-S-H | Calcium-Silicon-Hydrate |
| CV | Coefficient of Variation, % |
| D | Diameter, inch |
| $D_{avg}$ | Average Diameter, inch |
| E | Young's Modulus, ksi |
| EDS | Energy-Dispersive Spectroscopy |
| F | Load, Applied Force, lbf |
| $F_f$ | Frictional Load, lbf |
| $F_\tau$ | Shear Load, lbf |
| NP | Nanoparticles |
| SEM | Scanning Electron Microscopy |
| t | Thickness, inch |
| $\mu_s$ | Coefficient of Static Friction |
| $\sigma_{tensile}$ | Tensile Strength, psi |
| $\sigma_{Tensile\ Bond}$ | Tensile Bond Strength, psi |
| $\sigma_{UCS}$ | Unconfined Compressive Strength, psi |
| $\tau$ | Shear Stress, psi |

# CHAPTER 1

# INTRODUCTION

As it pertains to the oil and gas industry, cement plays a vital role in the life of a well. Whether used as a plug or in the wellbore annulus; shallow or deep, the cement that is placed must provide the structural fortitude to maintain its seal between both the wellbore and the environment, as well as in between zones. All while providing support and stability to the casing. The cement is then further tested as both natural and operational forces act on the casing-cement system that induce stresses within the cement body and at its bonded interfaces. These stresses tend to exploit the brittle nature of cement and lead to tensile failure of the cement sheath or even deboning from the steel casing, and as a result, the seal it is meant to provide is lost.

In an effort to prevent the leaking of a well or migration of formation fluids along the annulus, lab testing of wellbore cements enhanced with nano variants of wellbore cement additives has been conducted using both standard and novel testing procedures. The parameters studied were the compressive and tensile strengths using the standard unconfined compressive strength, (UCS), and Brazilian tensile strength testing methods. In addition, bond strength of the cement to a steel substrate was evaluated for both shear and tensile strength to investigate the impact nanoparticles have on cements ability to adhere to steel casing. The shear bonding strength test utilized a modified split core apparatus that was derived from similar testing (Zhang et al., 2016) and analyzed an induced failure plane of 75° from the horizontal using a testing setup fabricated for the purpose. Tensile bond strength testing was conducted using a new and novel method that utilized a similar

steel substrate to the shear tests for bonding purposes, as well as a steel connection point that was adhered to the top of the cement sample using a two part epoxy. This allowed the load frame to connect to the cement side without creating high load points that would fail before the bond.

This thesis aims to describe the mechanical response of a heavy, field ready cement with nanoparticle barite or magnetite introduced as a weight replacement in concentrations of 1%, 3%, and 5% by weight of cement (BWOC). By substituting small fractions of the original weighting agent, (standard barite), for the nanoparticle additives, the cements density remained relatively constant. This allowed for comparison across all of the samples under the assumption that the cement was designed for the same well conditions as the base case mixture, which had no nano additives. Furthermore, by assessing the compressive strength, tensile strength, and bonding strength with steel, inferences can be drawn regarding the potential performance of this cement under a wide range of loading conditions.

Chapter 2 gives a comprehensive literature review of the loading conditions faced by wellbore cement as well as the impact previous studies have observed when nanoparticles are introduced to various cements and concretes; as well as the bonding mechanisms observed between cement and steel. The materials used and sample preparation procedures followed are presented in chapter 3, followed by the lab testing procedures in chapter 4; the results observed and discussion in chapter 5; and the conclusions drawn are found in chapter 6.

# CHAPTER 2

# LITERATURE REVIEW

As of 2017 there was an estimated 4 million oil and gas wells drilled worldwide. It has been further suggested that between 1.9% and 75% of those wells have experienced some form of integrity failure (Jumenez et al., 2016). In other words, the low estimate for wells that are leaking or have potential to be leaking is upwards of 76,000. Outside of the obvious environmental impacts, the loss of zonal isolation can lead to costly repairs, downtime during wellbore construction, damages to downhole artificial lift equipment (Nelson and Guillot, 2006 p. 19), and losses in production that ultimately drives down the net income per unit produced. The overall result of leaking wells is of course unacceptable, and efforts the world over are being made to fix this problem from several directions.

## 2.1. FAILURE MECHANICS OVERVIEW

Praised for its high compressive strength capabilities, cement has been the barrier of choice from the beginning and even as its compressive potential grows, we still see failure in wells that were thought to be correctly designed. In order to determine potential solutions we must first understand the mechanisms that are causing the failure. To accomplish this, several studies have been conducted to look at the loading conditions faced by the cement sheath over the course of its life and then in turn attempt to describe the response of the cement to these changes. Earlier work has described several common loading scenarios that exploit the brittle nature of cement and cause

failure due to excessive tensile loading or debonding from the casing string. During high pressure operations where the wellbore pressure is dramatically increased, a linear relationship has been described between this pressure and the tangential tensile stresses induced in the cement (Thiercelin et al., 1998). Similarly, when the wellbore pressure decreases, as is the case with artificial lift operations (Nelson and Guillot, 2006 p. 19), the radial tensile stresses in the cement sheath increase linearly and is highest at the material interfaces which leads to debonding. Furthermore, in mature fields when high wellbore temperatures for steam injection are applied a high thermal gradient across the casing-cement-formation system is briefly established. This thermal gradient affects the cement sheath such that the inner portions closest to the casing expands faster than the cooler, outer portions closest to the formation. This non-uniform expansion is due to the low thermal conductivity of the cement and causes high tangential tensile stresses at the cement-formation interface that have the potential to cause both debonding at the formation and radial cracking through the cement sheath. These failures have been described as a function of the mechanical properties of the set cement and formation, as well as the geometry of the cased wellbore (Thiercelin et al., 1998). Unconventional lab testing aimed at simulating operations during the life of the well has shown that cyclic loading both physically on the cement itself and pressure fluctuations on the annular seal as well as repeated impacts caused by pipe whip during drilling can contribute to loss of zonal isolation (McDaniel et al., 2014).

The 2014 study by McDaniel et al. investigated two field cements used in the Marcellus shale play that were both designed to prevent gas migration in the intermediate section of the well, but saw very different success rates in practice. This is because when designing the cements to seal the well, the focus was placed on the short term isolation characteristics as opposed to the long

term. Meaning that while both cements were designed to have similar properties up to the point of hardening, once hydrated the cements took on very different mechanical characteristics. To address this, experimental procedures attempting to simulate the cyclic stresses associated with drilling, completion, and production operations were established. The tensile strength of the cements were examined using the routine split core method, while more complicated and unconventional tests were used to evaluate other mechanical properties. Anelastic strain of the samples was evaluated by cyclically loading the cores between 5-50% of their ultimate compressive strength to measure the residual strain of the core. Similarly, the annular seal durability was investigated by creating a lab scale annulus and cyclically pressurizing one side between 5,000-10,000psi until leakage was observed. An attempt at mimicking pipe whip was even made by repeatedly dropping a 66-gram steel ball onto a beam specimen from a fixed height until failure. In all cases, the more successful of the field cements outperformed the lesser, which goes a long way in proving that when designing a cement to prevent fluid migration, the mechanical properties of the hardened cement needs to also be taken into account if perfect zonal isolation is to be achieved.

Recognition of the failure mechanisms described has led to a push in research aimed at increasing the overall durability of cements through nano scale additives. This push has been made both in and out of the petroleum industry and has seen great potential in nanomaterials like $CaCO_3, Fe_2O_3, Fe_3O_4, TiO_2,\ and\ SiO_2,$ as well as various fibers, carbon nanotubes (CNT), graphene oxide (GO) and graphene platelets all with varying degrees of success. Several of these additives have also been observed during hydration in an attempt to better understand how they interact with the various components in cement. It was observed that when added to a cement paste, nano- $TiO_2, SiO_2,$ CNT, and GO acted as a substrate for the formation of the main binder in cement,

C-S-H which generally took the shape of the underlying particle. Furthermore, the anatase phase nano-$TiO_2$ presented nano-crystalline regions with a fringe spacing of 3 Å roughly the same size of the nano-$TiO_2$ particle while the GO sheets formed similar nano-crystalline regions at its surface, but skewed to 3.1 Å the farther away it got (Li et al., 2017). This coating of nanoparticles with C-S-H binder is promising when evaluating the overall strength of the cement as well as its bonding effect to aggregates or casing.

## 2.2. COMPRESSIVE STRENGTH

Classically speaking, the most common property used to determine the mechanical viability of a cement is its compressive strength. While we now know that compressive strength may not directly correlate to the success or failure of a primary cementing job, that isn't to say it shouldn't be considered because as we have already seen, increases in the formation pressure puts the cement sheath in an overall state of compression (Thiercelin et al., 1998). In order to maintain the integrity of the well, cements subjected to extreme forms of this scenario need to be able to withstand these pressures and as the industry drives towards drilling deeper wells, this scenario could become a reality with increasing frequency. To combat these mounting pressures, the application of a variety of nanomaterials have been identified to increase the compressive strength.

### 2.2.1. $SiO_2$ NANOPARTICLES

One of the more extensively investigated nanomaterials is $SiO_2$ nanoparticles, (SN). Being that silica is the major component of a pozzolan, SN are an enticing prospect when considering cement improvement and not without just cause. Previous studies in concrete research seem to be

in agreement that when relatively small concentrations of SN is added to a cement composite, an increase in compressive strength is seen (Jo et al., 2007; Li et al., 2004; Najigivi et al., 2013). Furthermore, the mechanisms responsible for this have been verified both visually using SEM, or scanning electron microscopy, (Jo et al., 2007; Li et al., 2004), as well as indirectly using the data provided by the heat evolution of the hydrating cements (Jo et al., 2007). From an optical perspective it was seen that the SN altered the microstructure in two key ways. The first and simplest of which came as a benefit of the particle's size in that they were able to fill voids too small for traditional particles (Jo et al., 2007; Li et al., 2004). This increased the packing efficiency of the hardened cement and reduced the porosity that is the typical mode of cement compressive failure. The second, and possibly more important change seen, was that SN acted as a promoter for the pozzolanic reaction with $Ca(OH)_2$ which in turn lead to the additional formation of C-S-H. It is important to note here that this same principle applies to silica fume, but because silica fume has a much smaller Blaine fineness value that the pozzolanic reaction rate is proportional to, it does not react as effectively as SN. This observation was also verified by observing the rate of heat evolution of the hydrating sample over 72 hours and it was found that the SN specimen released more heat when compared to both silica fume and an ordinary Portland cement (OPC) reference. In other words, the higher rate of heat evolution and shifted peaks signal an increase in the reactivity within the cement that can be traced back to the accelerated pozzolanic reaction (Jo et al., 2007).

### 2.2.2. $Fe_2O_3$ AND $Fe_3O_4$ NANOPARTICLES

Iron based nano-additives have also been a point of interest for improving cement strength. Because of their innately high compressive strength coupled with the high surface area to volume ratio of being on the nano scale, $Fe_2O_3$ or hematite nanoparticles (HN), and $Fe_3O_4$ or magnetite

nanoparticles (MN) have been studied as potential cement strengthening additives. Studies in general seem to be in agreement that in certain concentrations, both additives improve the compressive strength of cement, though an optimal concentration of either has seen little in the way of agreement. What is shared between all of the studies however, is the idea that both particles hold large amounts of water on their surface which naturally makes them foreign nucleation sites for hydration products to form while also filling what would have been pore space. Thereby improving the packing efficiency of the cement (Horszczaruk, 2019; Li et al., 2004; Khoshakhlagh, Nazari and Khalaj, 2012; Soltanian et al., 2015).

Moreover, studies concerning the effect of HN in cement have been conducted more broadly and have seen that concentrations as low as 3.09% and as high as 11.81% by weight of cement provide the highest compressive strength (Li et al., 2004; Soltanian et al., 2015). Additionally, visual observations with SEM has verified HN to act as nanofillers within the cement pore spaces while also noting their restrictive behavior on the growth of $Ca(OH)_2$ crystals thereby increasing the density of C-S-H hydration products (Khoshakhlagh, Nazari and Khalaj, 2012; Li et al., 2004).

### 2.2.3. $CaCO_3$ MICRO- AND NANOPARTICLES

Originally identified as an environmentally friendly partial volume replacement for cement, $CaCO_3$ has also been considered as a strength enhancing additive when ground to a smaller scale. One such study considered the effect of both micro and nanoparticle $CaCO_3$ in early-age ultra-high-performance concrete. They found that the highest compressive strength for a 24 hour set time at 50°F resulted from samples with 2.5% nanoparticle $CaCO_3$ along with 5% micro particle

$CaCO_3$ which showed a 76.8% improvement on the reference. Additionally 28 day samples at the same temperature showed the highest compressive strength to be that of samples with 5% concentration of nanoparticle $CaCO_3$ only and they showed 23.7% improvement on the reference. Interestingly, when cured at 68°F, the highest compression strength occurred at a concentration of 2.5% nanoparticle $CaCO_3$ for 24 hours (61.9% improvement) and 2.5% micro particle $CaCO_3$ for the 28 day set (5.4% improvement). It was concluded that the improvement in compressive strength was provided by a combination of a more efficient packing structure as well as the promotion of hydration reactions earlier in the process as compared to the reference. The latter explains why the performance at 24 hours was dramatically better in comparison to the reference than that of the 28 day cement (Camiletti et al., 2013). Another study completed on the subject of nanoparticle $CaCO_3$ saw an optimal compressive strength for both 7 and 28 day specimens cured at 68°F at concentrations of 2% by weight of the binder. This resulted in 11.2% and 8.6% improvement respectively when compared to the reference (Liu et al., 2012).

## 2.3. TENSILE STRENGTH

Less extensively investigated and yet possibly more crucial than compressive strength is tensile strength; particularly in wellbore cementing. Given the low compression-tension ratio of cements, and keeping in mind the several modes of potential tensile stresses seen in a cement sheath (Thiercelin et al., 1998), increasing this property in a primary cement is paramount in achieving successful zonal isolation. The addition of nano-materials aid this effort in a variety of ways that include both physical reinforcements and physicochemical mechanisms. Nanofibers and nanotubes have been seen to improve the tensile strength by bridging and hindering the propagation of

nanocracks while also lending their increased Young's modulus and tensile strength to the cement as is the case with carbon nanofibers and carbon nanotubes with their main limitation being a tendency towards aggregation because of their high hydrophobicity (Jafariesfad et al., 2017). Additionally, an unnamed, medium length, fiber has shown a 20% increase in tensile strength at 20-50°C and 35% increase at 250°C when added in concentrations of 0.5% BWOC in cements intended for wells undergoing steam assisted gravity drainage. It is also interesting to note that this increase in tensile strength appeared to come at a slight cost to the compressive strength at concentrations above 0.3% (Iremonger et al., 2015). Materials such as graphene nanoplatelets and a variety of nanoparticles have also been seen to increase the tensile strength and their benefits are discussed in the remainder of this section.

### 2.3.1. $SiO_2$ NANOPARTICLES

Similar to how they improved the compressive strength of cements, SN has shown to improve the flexural strength by 28% after 7 days and 27% after 28 days at concentrations of roughly 5.26% by weight of binder (Li et al., 2004). While flexural strength does not necessarily translate to tensile strength, the acceleration of the pozzolanic reaction leading to more C-S-H binder and an absence of large $Ca(OH)_2$ crystals in the hydration product when viewed under SEM (Li et al., 2004; Jo et al., 2007) describes a more densely packed cement with much higher binding potential.

### 2.3.2. $Fe_2O_3$ AND $Fe_3O_4$ NANOPARTICLES

To a lesser extent than compressive strength, the effect of HN and MN on the tensile strength of cement has been evaluated. Split core testing carried out in 2012 by Khoshakhlagh, Nazari and Khalaj determined that a concentration of 4% by weight of binder in a 28 day self-compacting concrete resulted in a 1.5 MPa increase in tensile strength. They further concluded that this improvement was brought about by the acceleration of C-S-H gel in the early hydration stages as a result of the increased formation of crystalline $Ca(OH)_2$ on the foreign nucleation site provided by the HN that was then consumed and refined into C-S-H binder. It was also seen in the same study that the flexural strength also peaked at 4% by weight of binder in the same 28 day self-compacting concrete (Khoshakhlagh, Nazari and Khalaj, 2012). In a similar study, the flexural strength of a 28 day cement mortar saw a 17.8% and 23% improvement at HN concentrations of 3.09% and 5.26% by weight of cement respectively (Li et al., 2004). These results were then further investigated using SEM and reported the absence of large $Ca(OH)_2$ crystals at concentrations of up to 5.26%, which is in agreement with the conclusions drawn by Khoshakhlagh, Nazari and Khalaj.

In studies regarding MN, similar results have been seen as that of HN. In a study of a 28 day high strength concrete, a 26.3% increase in tensile strength was reported for concentrations of 1.5% when compared to the reference using the split core method (Shekari and Razzaghi, 2011). Additionally, a similar study found that a 28 day ordinary concrete saw a 25% increase in tensile strength at concentrations of 1.5% when compared to the reference (Jaishankar et al., 2015). Another study regarding the flexural strength of MN enhanced cement mortars at high temperatures found that concentrations of 3% and 5% yielded 8.5% and 9.76% improvement compared to the

base case at 20°C. It was also reported that at 200°C the same cement mortars saw 11.58% and 5.26% improvement in flexural strength when compared to the reference (Sikora et al., 2018). These results show not only an increase in the tensile strength, but also a resistance to elevated temperatures with the incorporation of MN.

### 2.3.3. GRAPHENE NANO PLATELETS

Alkhamis' 2018 study also reported improvement to the tensile strength of class H Portland cement across the same concentrations of graphene nano platelets while undergoing Brazilian tensile testing. It was stated that by adding just 0.1% BWOC, the tensile strength improved at least 20% when compared to the reference and in when 0.9% was added, a 44.9% improvement was observed (Alkhamis et al., 2018).

Something interesting to note here is that so far it has been seen that nanoparticles have a tendency to improve the strength of cementious materials by two main methods. They increase the packing efficiency of the microstructure and promote hydration through either presenting silica to the system, acting as a nucleation point or accelerating the growth of $Ca(OH)_2$ crystals thereby promoting their consumption resulting in more efficient production of C-S-H binder. This typically sees a dramatic increase of compressive strength and a lesser improvement on the tensile strength, but with graphene nano platelets the opposite is shown. The reasoning for this can be speculated as an effect of the platelets' high length to width ratio, or aspect ratio. Similar to how the addition of nanofibers increased the tensile strength of cements by mitigating the propagation of nanocracks. It is possible that the additional tensile strength seen in the cement is a result of the nano platelets bridging nanofractures and holding off failure past the actual tensile strength of the cement binder.

## 2.4. CEMENT / STEEL BONDING

As discussed in section 2.1, pressure and temperature fluctuations put large amounts of stress at the casing-cement casing and cement-formation interfaces. The cement contact along this plane consists of a mostly constant structure of segregated hydration products once cured (A. J. Majumdar et al., 1978). As such, the composition of this hydration product, as well as the surface condition of the substrate play key roles in the strength of the bond that is formed.

### 2.4.1. WELLBORE CEMENT / STEEL BONDING

In the way of wellbore cement to steel bonding, very little work has been done; however, studies on the subject seem to agree on one simple fact. The rougher the surface is, the stronger the bond it forms with cement will be. L. Carter and G. Evans tested the shear and hydraulic bond strength of a lab scale annulus across a matrix of pipe finishes, drilling fluids, and stimulation stresses proved this in a 1964 study (Carter and Evans, 1964). They concluded the study by pointing out that a rough, water wet surface always provides the strongest bond and that the hydraulic strength of the bond is primarily a function of pipe geometry changes. A more recent study reached the same conclusion when comparing the shear bond strength of polished, sand blasted, and rusted steel surfaces. After analyzing the surface roughness of each case using a profilometer, they used a modified form of a split core setup and tested each at angles ranging from 0° to 25° from the vertical. They concluded that no matter the drilling fluid or spacer used, the rusted surface always provided the strongest bond with cement because its increased roughness created better mechanical interlocking (Zhang et al., 2016).

Using particle probe scanning force microscopy, (SFM), it has also been observed that in early hydrated cement, $Ca(OH)_2$ exhibits significantly lower bonding strength to steel microspheres than the other hydration products (Li et al., 2018). It was concluded that the irregular crystals $Ca(OH)_2$ forms do not create effective contact with the steel and so a weaker bond is created. As such, reducing the amount of $Ca(OH)_2$ present in the hydrated cement could allow for the formation of a stronger bond at the cement-steel interface.

### 2.4.2. EPOXY BASED CONCRETE NANOCOMPOSITE BONDING

Outside of traditional cementing, one notable study focused on how various nanoparticles influenced the bonding ability of polymer based concretes using the slant shear testing method. This 2017 investigation by A. Douba et al. saw a 51% increase in the bond strength between the polymer concrete nanocomposite when compared to the neat polymer concrete. It was speculated that this improvement came about as a result of chemical reactions between the aluminum nanoparticles and the –OH groups formed on the sandblasted steel surface (Douba et al., 2017).

# CHAPTER 3

# MATERIALS AND SAMPLE PREPARATION

## 3.1. MATERIALS

The base cement used for comparison was designed to be similar to what would be seen used in actual primary cementing applications. It consisted of a class H cement and simulated seawater with a water to cement ratio of 0.396 as determined by previous hydration testing (see appendix A for details). The additives then included D-air 5000, which acted as a de-foamer; hydroxyethylcellulose (HEC) which acted as a fluid loss control agent; and standard barium sulfate (barite) that acted as both a standard weighing agent as well as a source of weight replacement for the nanoparticle additives. This weight replacement acted as a means to maintain roughly the same cement density while still adding concentrations of nanoparticle additives.

While little work has been done in the way of nanoparticle barite or magnetite specifically as a wellbore cement additive, studies on the effects of other nanoparticles could give an indication of their impact. In general, it has been seen that nanoparticles increase the packing efficiency of setting cements by filling voids created between larger particles (Camiletti et al., 2013; Jo et al., 2007; Li et al., 2004). Moreover, the high surface area of nanoparticles has been seen to hold large amounts of water that creates a foreign nucleation sight for hydration products further filling pore space and restricting the growth of $Ca(OH)_2$ crystals thereby increasing the density of C-S-H

hydration products (Horszczaruk, 2019;Khoshakhlagh, Nazari and Khalaj, 2012; Li et al., 2004; Soltanian et al., 2015).

### 3.1.1. NANOPARTICLE BARITE

In industry cements, standard barite is used as a readily available weighing agent for cements up to 19ppg. (Nelson and Guillot, 2006 p. 70). Additionally, when applied to wellbore cementing, additional water is required to wet its particles, which is typically 0.024 gallons per pound of barite added. For this reason, it was initially decided that for the nanoparticle variation of this additive, an increase in the water requirements would be necessary due to the increased surface area. The additional water required was determined through hydration testing using the vortex method outlined in appendix A and was found to be 0.216 gallons per pound added. In a typical wellbore cement, the addition of water required by barite leads to cements with lower compressive strengths, and as such, the addition of almost 10 times that water could hinder any strength improvement seen in the cement. As a result, preliminary trials saw an increase in void space within the sample that ultimately reduced the overall strength of the cement body. A detailed account of this can be found in appendix A. Final recipes did not incorporate extra water and used the standard field water requirement for barite as a guide.

### 3.1.2. NANOPARTICLE MAGNETITE

While not as widely used, iron based weighing agents such as hematite and magnetite are very efficient weighing agents for wellbore cements due to their low water requirements and high specific gravity. In the current study, nanoparticle magnetite with an average diameter between 50-

100nm as verified by the manufacturer through SEM is used. Though it clearly has a high surface area that will hold large amounts of water, the decision was made not to add additional water to the recipe. This is because there is no current field standard for magnetite, and while the closest seen is hematite that requires 0.0023 gallons per pound added, other iron based additives such as iron carbonate have no water requirements in the field due to their low concentrations. Further testing on this should be done however, to investigate the effects of additional water in this slurry and its effects on mechanical strength, pumpability, and setting time.

## 3.2. SAMPLE PREPARATION

For all of the testing, the cement slurry was prepared in the same manor; however, each test required its own specific sample preparation, and is discussed in further detail in their respective sections.

### 3.2.1. SLURRY AND CORE PREPARATION

Each sample was mixed using the recipes described in Table 1 and prepared according to API 10A/ISO 10426-1:2000 with a handful of notable exceptions.

**Table 1 - Cement recipes used for testing.**

| | Sample Recipes | | | | | | | | | |
|---|---|---|---|---|---|---|---|---|---|---|
| | Cement Mass (g) | Seawater Mass (g) | Boric Acid Mass (g) | Defoamer Mass (g) | Barite Mass (g) | HEC Mass (g) | NP Barite BWOC (%) | NP Barite Mass (g) | NP Magnetite BWOC (%) | NP Magnetite Mass (g) |
| Heavy Base Case | 850 | 362.7 | 3.4 | 1.3 | 100 | 4.25 | - | - | - | - |
| 1% NP Barite | 850 | 362.7 | 3.4 | 1.3 | 91.5 | 4.25 | 1 | 8.5 | - | - |
| 3% NP Barite | 850 | 362.7 | 3.4 | 1.3 | 74.5 | 4.25 | 3 | 25.5 | - | - |
| 5% NP Barite | 850 | 362.7 | 3.4 | 1.3 | 57.5 | 4.25 | 5 | 42.5 | - | - |
| 1% NP Magnetite | 850 | 362.7 | 3.4 | 1.3 | 91.5 | 4.25 | - | - | 1 | 8.5 |
| 3% NP Magnetite | 850 | 362.7 | 3.4 | 1.3 | 74.5 | 4.25 | - | - | 3 | 25.5 |
| 5% NP Magnetite | 850 | 362.7 | 3.4 | 1.3 | 57.5 | 4.25 | - | - | 5 | 42.5 |

The first two deviations from the standard regarded the time of mixing and molding procedures. The standard procedure is 15 seconds at 4000 RPM ±200 RPM with the fluid components already in place and the solids added in this time frame; followed by 12000 RPM ±500 RPM for an additional 35 seconds. The addition of nanoparticles, however, saw an increase in the amount of clumping when the solids were added. Because of their tendency to tie up water on their surface, full introduction of the solids became difficult because they would build up on the fluid surface while the liquid underneath simply swirled without much mixing taking place. It was seen that extra time during the low RPM phase was required along with tapping on the cup and even gentle shaking to bring the liquids and solids into a homogeneous state. This extra time typically ranged from an additional 30-40 seconds and was always followed by the standard high RPM phase for 35 seconds. In an effort to more efficiently disperse the nanoparticles, they were added during the low RPM stage prior to the rest of the solids. Once mixed the samples were poured into clean molds that were 2 inches in diameter by 4 inches in length and stirred with a thin metal rod while being subjected to external vibration until bubbles stopped forming on the slurry surface to ensure there was no trapped gas to leave voids within the cement body.

The remaining difference in procedure from the standard was during and after the curing procedure. In lieu of a water bath at 170°F, a brine of pH12 NaOH solution at 194°F was used to mimic the deep well environment that the cement would be exposed to and promote hydration with an elevated pH without worry of unintentional reaction with the cement. From there the samples were pulled from the oven and left to cool with the fluid. This procedure deviates from the standard in that a controlled water bath is not used. Instead, it was verified that the rate of cooling does not exceed that which is specified in API 10A by monitoring the fluid temperature near the cores in a

trial that used the same fluid and wrapping procedure. Once cooled, the cores were prepared according to the testing to which they will be subjected.

The samples that were aged at 194°F were allowed to harden for 48 hours before being removed from their molds and placed in the NaOH hydration solution. From there they were placed in the oven and left to cure for 28 days to add up to a sum of 30 days ageing before being prepared for testing.

### 3.2.2. COMPRESSIVE STRENGTH SAMPLES

The unconfined compressive strength (UCS) cores were prepared and cured as described in the previous section. Once the desired cure time had elapsed with time to cool, the ends of cores were leveled using a tile saw to cut away a thin layer. From there, the ends of the cores were then ground using 80 and 120 grit sand paper sequentially to ensure the core ends were parallel to within 0.03 inches of any three measurements taken. The faces of each end were then polished using 2000 grit sandpaper to remove any potential points of high load concentration. Lastly, the cores were returned to the NaOH solution until it was time in order to test to avoid drying.

### 3.2.3. TENSILE STRENGTH SAMPLES

Each core was cut into 3, 1-1/4 inch sections and then ground down to 1 inch such that the thickness of any three measurements deviated less than 0.008 inches. While not an official standard, this limit was set by interpolating the allowable deviation set in ASTM C496/496M-17, which describes that the length of the split core shall not differ more than 5% in length. It is important to note here that due to blade walk during the cutting of the samples, some of the faces were too far

from parallel to be ground down into the desired range of thickness. Grinding of these samples was stopped when one edge measured below 1-inch thickness while any other edge measured both over 1 inch and above the 0.008-inch deviation threshold. This was then recorded to be further evaluated in the post testing analysis.

### 3.2.4. SHEAR BOND STRENGTH SAMPLES

The samples to be tested were created by first dry brushing the sand blasted coins in accordance to ASTM C882/C882M to ensure that each coin provides a surface of similar roughness for the cement to bond to; thereby decreasing any variation between samples. From there the coin was positioned in the bottom of a plastic core mold that was then capped. The cement was then mixed as described in section 3.2.1 and poured into the mold using a marked rod to ensure the cement is roughly 0.394 inches (1cm) thick (Zhang et al., 2016). Once the cement is placed in all of the samples of the sample set, a layer of DI water was added to the top to prevent the sample from drying that could lead to shrinkage. The samples were then sealed using the mold caps, numbered in the order they were made, and left to set for 72 hours at ambient conditions so that they would be tested at the same age as the tensile bond strength samples.

### 3.2.5. TENSILE BOND STRENGTH SAMPLES

The samples used to evaluate the tensile bond strength of the cement to steel interface were created by first preparing the steel substrate by sandblasting in accordance to ASTM C882/C882M. With the steel ready, a neoprene washer was lightly coated with enough grease on one side to

prevent fluid loss between it and the steel substrate, but not so much it squeezed out and interacted with the cement. This was used as a way to restrict the contact area between the steel substrate and the cement; which in turn increased the rate at which stress accumulated at this point in comparison to the rest of the cement body (see Figure  for details). Next, the mold was put into place and the slurry was poured to fill the bottom two inches of each mold. Immediately after pouring, the slurry a layer of DI water was applied, and the sample was left to harden for 48 hours.

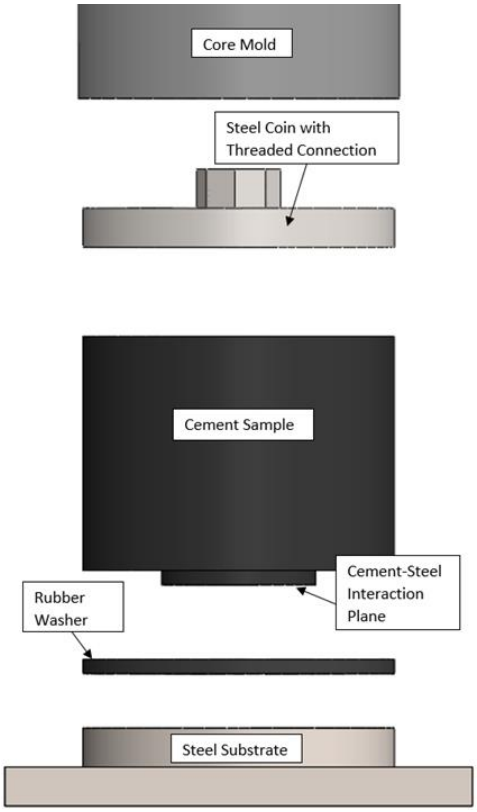


**Figure 1 - Tensile bond testing sample model.**

At the end of this period the samples were removed from their molds and the cement tops were trimmed using a tile saw in order to provide a flat, even surface to attach the upper connection point. Once cut, the samples were rinsed of residual cuttings using DI water, and gently dried using

a paper towel. The sample tops were then briefly rinsed with acetone to remove any excess moisture from the relatively porous surface, and once again gently dried with a paper towel. After completing this process, the samples were then placed in a shallow bath of DI water that covered most of the sample, but allowed the tops to remain exposed to air and therefore dry.

After an hour drying period, each sample was removed and a high strength, two-part epoxy was then mixed and applied to the surfaces of both the cement top and the steel connection point. The two components were then pressed together by hand until excess epoxy was seen to be pressed out of their interface in order to ensure total coverage between the two faces. Lastly, the sample was returned to the water bath and given 24 hours for the epoxy to cure.

# CHAPTER 4

# TESTING PROCEDURES AND DATA COLLECTION

## 4.1. COMPRESSIVE STRENGTH

Prior to testing, the dimension of a specimen was measured to the nearest $1/1000^{th}$ of an inch using calipers and recorded for three points roughly 120° from each other. Because the molds used to make the cores are known to be within the tolerances set by ASTM C192/C192M, only one sample from each sample recipe set was measured for diameter. The cores were then loaded using a constant displacement rate that was 0.5% of the sample length per second. This displacement rate was selected after testing various rates and calculating their applied stress on the sample. See section 4.1.1 for further details.

Once failure occurred, several images of the sample still under load were taken and the loading data was recorded. The peak load is then applied to Equation 1 using the dimensions recorded before testing.

$$\sigma_{UCS} = \frac{4F}{\pi D^2}$$

**Equation 1 - Calculation for unconfined compressive strength.**

### 4.1.1. Displacement Rate Testing

In order to establish a displacement rate within the 35±7psi stress rate outlined in standard ASTM C39, a series of preliminary tests were conducted. Routine compression tests were carried out at displacement rates of 2%/s, 1.5%/s, 1%/s, and 0.5%/s; and the results were plotted and analyzed on a stress over time basis by fitting a line to the elastic region of the plot (see Figure 1). The slope of this line was then used as the average rate of stress on the sample and using this, it was determined that the best rate of displacement for testing would be 0.5%/s.

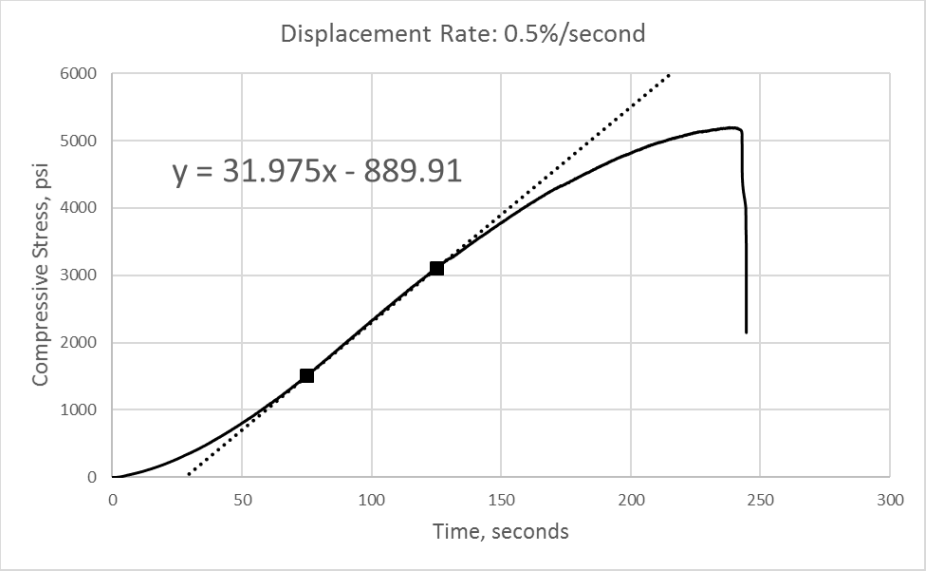


**Figure 1 - Stress over time plot used to determine stressing load rate at given constant displacement rates.**

## 4.2. TENSILE STRENGTH

The Brazilian Method was used to indirectly test the tensile strength by applying a compressive load across the diameter of a thin disk whose diameter was roughly double its thickness. The compressive load at failure was used to calculate the tensile strength using Equation 2.

$$\sigma_{tensile} = \frac{2F}{\pi D t}$$

**Equation 2 - Tensile strength calculation for Brazilian testing.**

Immediately prior to testing, the sample was removed from the hydrating solution, gently dried with a paper towel and measured for thickness and diameter using calipers. Each measurement was taken roughly 120° from each other and recorded to the nearest 1/1000th of an inch to insure that any deviation in the thickness or diameter could be detected. From there, sample was centered on the curved platens detailed in appendix C; as shown in Figure 2. Once in place the sample was loaded using a constant displacement rate of 0.005 in/min that resulted in start to finish testing times in the 2-3 minute range (García et al., 2017). A brief description of the procedure used to find this displacement rate is provided in section 4.2.1. The test was stopped manually once failure occurred and pictures were taken of the sample still under the load applied after stoppage for post testing analysis.

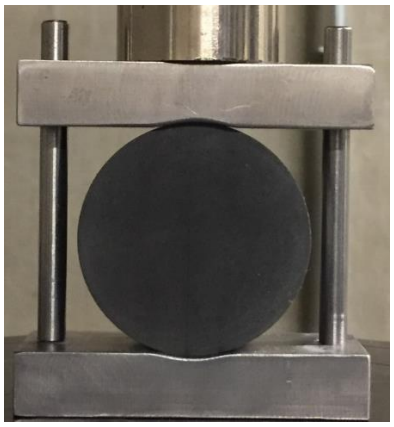

**Figure 2 - Brazilian disk specimen centered on curved loading platens.**

The validity of the results for each sample was considered primarily on the grounds that the primary fracture initiated both from the center of the disk, and was parallel to the loading axis as shown in Figure 3. The results whose samples did not exhibit this type of failure were excluded from further analysis.

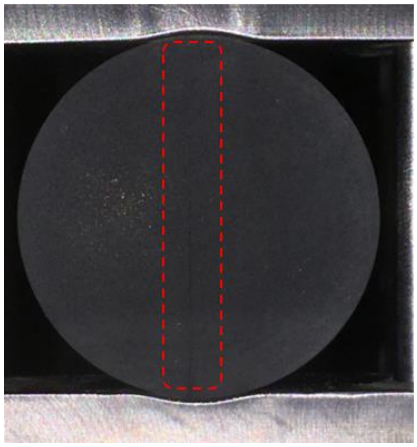

**Figure 3 - Brazilian disk specimen with failure parallel to loading direction.**

Once the testing was completed and the failure loads were recorded, the tensile strength was calculated using equation 4.1 as described above. The failure load was used as recorded, and the average of the three measurements taken for both the diameter and thickness were taken as their respective parameters. From there, the resulting strengths were analyzed for their deviation from the mean and how that relates to the visually analyzed failure mode, as well as the thickness deviation. This was done to distinguish correctly, the data to be used that describes any trends between samples.

### 4.2.1. Displacement Rate Testing

To establish the ideal displacement rate that would result in failure within 2-3 minutes (Garcia et al., 2017), several samples were tested under different displacement rates. In the 2017 study by Garcia, a constant displacement of 0.2 in/min was used on 150mm (5.9 in) diameter cores. Because the cores used in this study were nearly 30% of that size, the stress would develop much quicker, resulting in earlier failure. With this in mind a starting displacement rate of 0.0236 in/min was used followed by 0.01 in/min and 0.005 in/min. It was seen that failure occurred in the desired time frame only when the displacement rate was reduced to 0.005 in/min and this rate was selected for the remainder of the testing. All of the results are shown below in Figure 4.

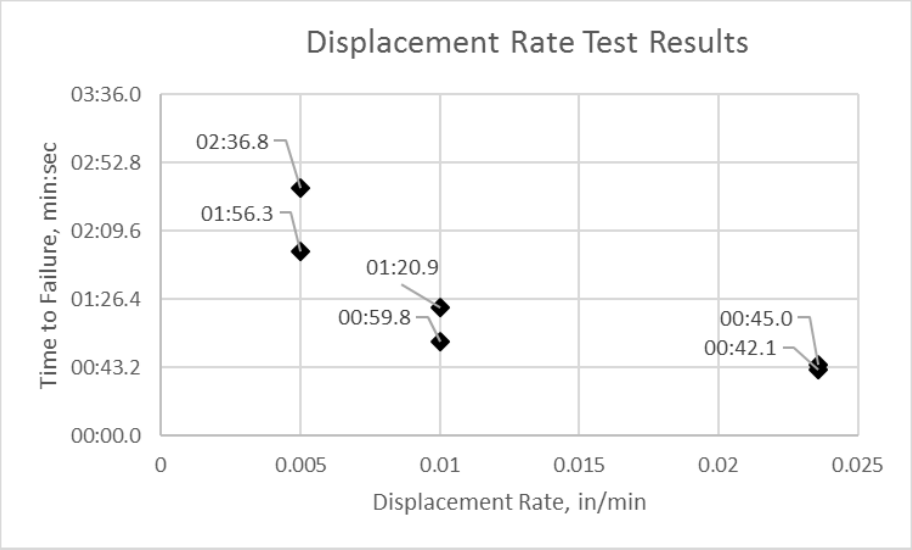


**Figure 4 - Time to failure of Brazilian disk samples at different loading rates.**

## 4.3. SHEAR BOND STRENGTH

In order to test the effect of nanoparticles on the shear bonding strength between cement and steel, a slightly altered version of the setup used in Zhang's 2016 study was designed and fabricated. This apparatus imposes a failure plain on the specimen by loading the core at varying degrees away from the centerline of its two halves as indicated by the loading platens around its circumference as seen in Figure 5.

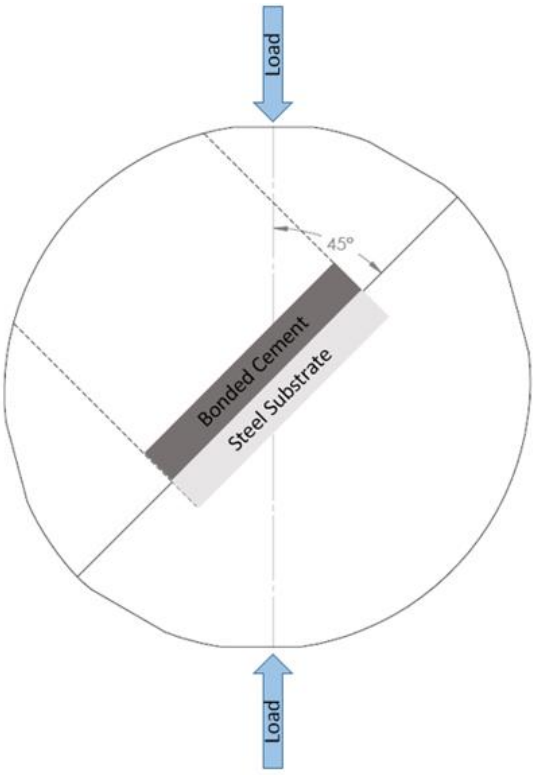


**Figure 5 - Detailed sketch of shear bond strength testing apparatus working principles.**

In between testing sets, the interacting plane of the core holders was refinished and polished to remove any blemishes and reduce the potential effect of the friction seen there. Additionally, prior to each test, the faces of the interacting plane were wiped clean using a paper towel, and a thin layer of mineral oil was applied to further reduce the friction.

At the end of the 72-hour curing period, the samples were tested chronologically according to their designated sample number. Each sample was first drained of their residual DI water, and removed from the mold by uncapping the bottom end of the mold, applying pressure to the sample from the cement side using a length of hardened wood, and pulling the mold off of the sample. This

was determined to be the best sample removal method to prevent any damage to the sample prior to testing. Once removed the samples resembled the one seen in Figure 6.

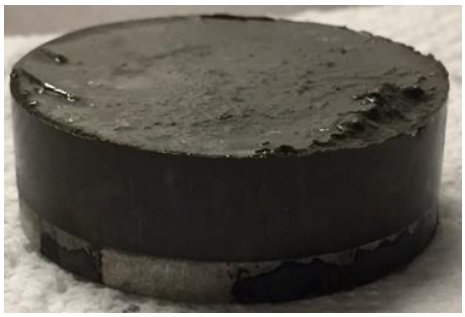

**Figure 6 - Shear bond strength sample.**

The sample was then placed in the steel coin side of the sample holder and the cement side was placed over it, taking care to make sure that the loading platens were aligned correctly and the faces of the sample holder halves mated correctly. From there the setup was placed onto the load frame at the desired angle as shown in Figure 7.

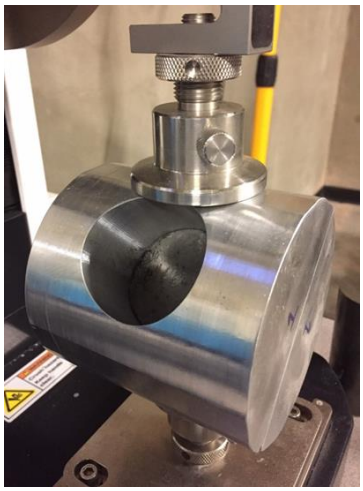

**Figure 7 - Shear bond strength testing apparatus ready to begin test.**

With the sample in place, the test was started and continued until failure. Because of the expected low values of the bond strength, and the geometry of the set up being similar to a split core test, it was initially decided to stray from the loading procedure recommended in ASTM C882/882M and use the constant displacement rate of 0.2 in/min recommended for Brazilian testing (García et al., 2017). It was seen, however, that this displacement rate was too high and caused rapid loading of the sample which is both dangerous, and likely to produce unreliable results due to the rapid loading. The displacement rate was then reduced to 0.02in/min which resulted in gradual loading and failure within a more favorable time window. It was seen, however, that testing at this load rate took several minutes to complete which in turn lead to concerns about fatiguing the bond. Further investigation revealed that in a study evaluating the adhesive strength between concrete and steel reinforcement bars, a displacement rate of 0.05mm/s was used for three separate methods (Józef Jasiczak et al., 2017). Because its proven applicability and relatively low displacement rate, 0.05mm/s (0.11811 in/min) was selected as the displacement rate for testing in this study.

Upon completion of each test, the recorded data was saved and images of both the steel coin and cement puck were taken for later analysis to verify that complete adhesion failure occurred (A. Douba et al., 2017). The recorded value for the load at failure was then used to calculate the shear strength of the sample using Equation 3, Equation 4, and Equation 5. Initially, it was assumed that the friction between the interacting aluminum faces of the sample holder could be accounted for in the calculation step by using the normal force calculated from the failure load, and a friction coefficient ($\mu_s$) of 0.3 for lubricated aluminum-aluminum contact. This revealed two very important concepts in early testing that ultimately changed the procedure. First

and foremost it was seen that at a failure angle of 45°, the static friction between the two faces overcame the shear bond strength at the cement-steel interface. As such the resulting data gave the false impression of significantly higher shear bond strengths for the same cement sample set. This was particularly evident in samples of the heavy base case where the apparent shear bond strength at 45° was 92% and 112% higher than the results at 75° and 60° respectively; whereas there was only a 10% increase in apparent shear bond strength when going from 75° to 60°. For this reason, it was decided to omit any further testing at 45°. It should also be noted here that while 10% could be deemed inconsequential if comparisons were only drawn between samples tested at the same angles, the added normal force at 60° was seen to scuff the interacting planes of the aluminum surfaces. This increase in surface roughness then has potential to skew the results of tests thereafter, and so it was decided to only test samples at 75° from the horizontal.

$$F_f = \cos(\theta) * F * \mu_s$$

**Equation 3 - Calculation used to account for friction in shear bond strength testing.**

$$F_\tau = \sin(\theta) * F$$

**Equation 4 - Calculation used to determine the force applied parallel to the interacting plane during shear bond strength testing.**

$$\tau = \frac{(F_\tau - F_f)}{A}$$

**Equation 5 - Calculation used to determine the shear bond strength of the cement-steel interface.**

## 4.4. TENSILE BOND STRENGTH

Direct testing of the tensile bond strength was completed by first removing the sample from the water bath, gently drying it, and attaching the eye bolt to the threaded top connection. The steel base of the specimen was then slid into position on the steel base and connected to the eyebolt of the clevis bracket with a quick link. Once connected, the eyebolt in the clevis bracket was then adjusted until the load reads 1.0 lbf in order to verify that the sample was aligned and ready for testing. The eyebolt was then backed off slightly to reduce the applied load back to 0 lbf for the start of the test.

With everything in position, the samples were loaded until failure using a constant displacement rate of 0.05 mm/s (0.11811 in/min) in order to match the load rate of the shear bond tests. At the conclusion of each test, the time and applied load data was saved and the sample was analyzed for any indication of failure other than complete bonding failure [see Figure 8 and Figure 9 for details]. Any sample that was seen to fail away from the cement-steel interface was documented for further analysis.

**Figure 8 - Tensile bond strength post testing analysis revealing failure away from the material interface.**

**Figure 9 - Tensile bond strength post analysis of complete bond failure at the material interface.**

The tensile bond strength was calculated using Equation 6 as well as Equation 7 and assumed no losses from the testing set up. This point is important because variation seen between data is largely a function of surface roughness, as well as how fully the cement hydrates; and not

how the apparatus is aligned. It is also important to note that because the neoprene washer used to restrict the bonding surface was defined with tolerances of ±0.1 inches, the average diameter was determined by taking three measurements about the bonded surfaces circumference roughly 120° apart. See Figure 10 for details.

$$D_{avg} = \frac{D_1 + D_2 + D_3}{3}$$

**Equation 6 - Calculation used to determine the average diameter of the bonded interface.**

$$\sigma_{Tensile\ Bond} = \frac{F}{(\frac{\pi}{4} * {D_{avg}}^2)}$$

**Equation 7 - Calculation used to determine the tensile bond strength of cement-steel interface.**


**Figure 10 - Measuring the diameters to be averaged and used to calculate the tensile bond strength.**

CHAPTER 5

# RESULTS

The results from this project are presented in four sections that individually outline the effect each nano additive had on the respective mechanical characteristic. In general, testing showed that marginal changes of cements mechanical properties were made when employing nanoparticles. The following sections summaries of the results are described. For a thorough detailing of the results, please see appendix E.

## 5.1. COMPRESSIVE STRENGTH

UCS testing revealed very slight changes to the cements compressive strength. In general, it was seen that the compressive strengths of the cement was similar to what would be expected of a class H cement cured for 28 days. Namely, the base case cement yielded a mean UCS value of 5039 psi with a coefficient of variation (CV) of 5.9%. Please see Table F.1 in appendix F for details.

### 5.1.1. NANOPARTICLE BARITE

At concentrations of 1% and 3% BWOC, samples containing nanoparticle barite showed reductions of 3.7% and 3.6% in compressive strength with coefficients of variation of 9.6% and 22.5% respectively. Samples containing 5% BWOC nanoparticle barite saw an increase in compressive strength of 7.6% compared to the base case, with a variation coefficient of 6.2%. Please see Table 2 or details as well as Table F.2 in appendix F for all individual test results.

**Table 2 - Summarized UCS results for the nanoparticle barite samples.**

| | Mean UCS (psi) | CV (%) | Change from Base Case (%) |
|---|---|---|---|
| Base Case | 5039.1 | 5.9% | - |
| 1% NP Barite | 4854.8 | 9.6% | -3.7% |
| 3% NP Barite | 4863.1 | 22.5% | -3.6% |
| 5% NP Barite | 5439.2 | 6.2% | 7.6% |

### 5.1.2. NANOPARTICLE MAGNETITE

The largest improvement to the compressive strength seen in this study was observed in samples containing 1% BWOC nanoparticle magnetite. These samples were seen to yield 20.5% improvement on the base case with a coefficient of variation of 7.3%. Samples containing 3% BWOC concentrations proved to be a local minimum of improvement with only 8.9% increase on the base case followed by 5% BWOC who saw 19.2% improvement on the base case. As seen in the summarized Table 3, the change in the trend did not arise as a result in large sample variation. In fact, the variation narrowed as concentrations increased. A complete account of the individual test results are listed in Table F.3 under appendix F.

**Table 3 - Summarized UCS results for the nanoparticle magnetite samples.**

| | Mean UCS (psi) | CV (%) | Change from Base Case (%) |
|---|---|---|---|
| Base Case | 5039.1 | 5.9% | - |
| 1% NP Magnetite | 6187.6 | 7.3% | 20.5% |
| 3% NP Magnetite | 5507.2 | 5.4% | 8.9% |
| 5% NP Magnetite | 6110.5 | 4.1% | 19.2% |

## 5.2. TENSILE STRENGTH

Utilizing the Brazilian testing method for brittle materials as described in the previous sections, it was seen that nanoparticles within the cement could potentially be detrimental to its tensile strength. On average, the tensile strength of a sample was observed to be negatively impacted by any concentration of either nanoparticle additive when compared to the base case. Please see Table F.4 in appendix F for the base case sample results.

### 5.2.1. NANOPARTICLE BARITE

Samples containing 1%, 3%, and 5% BWOC concentrations of nanoparticle barite yielded reductions in tensile strengths of varying magnitudes when compared to the base case. As shown in Table 4, the largest change from the base case was observed in the samples containing 3% nanoparticle barite followed by 5% and 1% in order. All test results are available in Table F.5 under appendix F.

**Table 4 - Summarized Brazilian test results for the nanoparticle barite samples.**

| | Mean Tensile Strength (psi) | CV (%) | Change from Base Case (%) |
|---|---|---|---|
| Base Case | 1031.7 | 19.5% | - |
| 1% NP Barite | 927.4 | 19.8% | -10.6% |
| 3% NP Barite | 774.1 | 5.0% | -28.5% |
| 5% NP Barite | 898.8 | 10.3% | -13.8% |

### 5.2.2. NANOPARTICLE MAGNETITE

It was observed in samples containing nanoparticle magnetite that the nanoparticle concentration and tensile strength were inversely related. That is, as the concentration increased,

the mean tensile strength decreased proportionally. Table 5 details this trend and the individual test results are presented in Table F,6 under appendix F.

**Table 5 - Summarized Brazilian results for the nanoparticle magnetite samples.**

| | Mean Tensile Strength (psi) | CV (%) | Change from Base Case (%) |
|---|---|---|---|
| Base Case | 1031.7 | 19.5% | - |
| 1% NP Magnetite | 868.3 | 11.6% | -17.2% |
| 3% NP Magnetite | 851.5 | 9.9% | -19.1% |
| 5% NP Magnetite | 846.7 | 16.4% | -19.7% |

It is also interesting to note here, that while the mean tensile strength values for the magnetite samples are significantly different in relation to the base case; between the highest and lowest concentrations of nanoparticles, there is only a 2.5% change.

## 5.3. SHEAR BOND STRENGTH

The effect of the nanoparticle additives was most clearly demonstrated while evaluating the cements bonding potential with steel. In the shear bonding tests, improvements on the base case cement were seen in concentrations as little as 1% BWOC for both nanoparticle additives. Although the variation of results within sample is substantial, (8.8-38.5%), a trend between the concentration of nanoparticle additives and the shear bond strength is observed.

As summarized in Table 6, increasing the concentration of nanoparticle additives was seen to increase the shear bond strength of the interacting plane between the cement and steel substrate.

This correlation as represented by the trend line in Figure 11and Figure 12, demonstrates that the mean shear bond strength increases with concentration. Individual test results are available in appendix F and are represented by Table F.7, Table F.8, and Table F.9.

**Table 6 - Summarized shear bond strength results.**

| | Mean Shear Bond Strength (psi) | CV (%) | Change from Base Case (%) |
|---|---|---|---|
| Base Case | 63.8 | 17.7% | - |
| 1% NP Barite | 67.4 | 8.8% | 5.5% |
| 3% NP Barite | 76.7 | 29.6% | 18.4% |
| 5% NP Barite | 94.1 | 38.5% | 38.5% |
| 1% NP Magnetite | 68.5 | 10.1% | 7.1% |
| 3% NP Magnetite | 80.3 | 21.2% | 22.9% |
| 5% NP Magnetite | 102.7 | 19.2% | 46.8% |

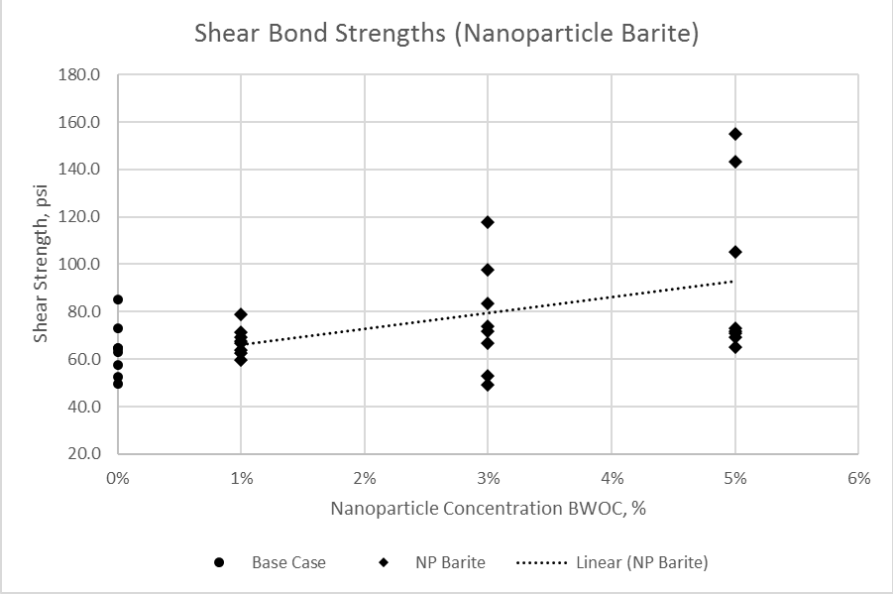


**Figure 11 - Shear bond strength plotted as a function of nanoparticle barite concentration (BWOC).**

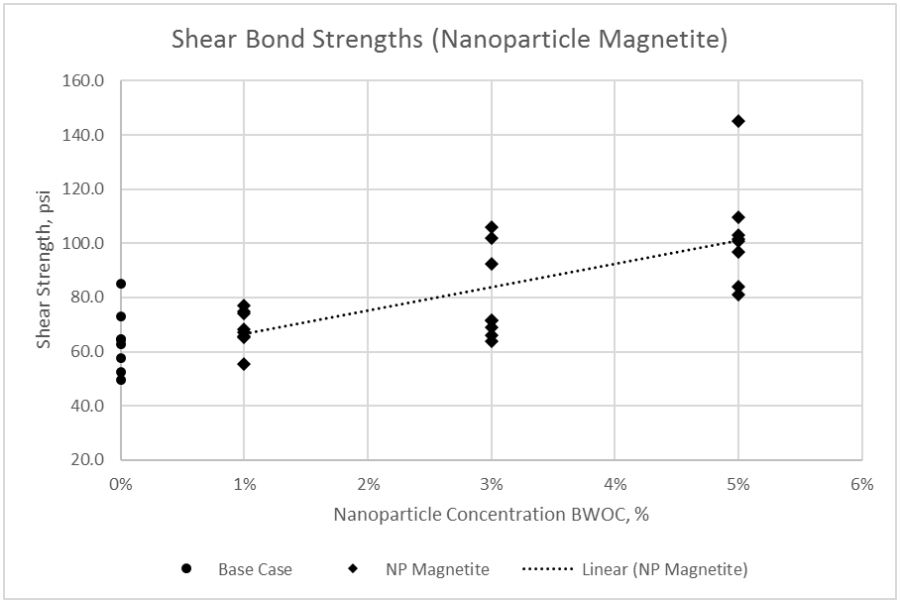


**Figure 12 - Shear bond strength plotted as a function of nanoparticle magnetite concentration (BWOC).**

All of the samples tested were visually confirmed to have failed at the material interface similar to the example shown in Figure 13.

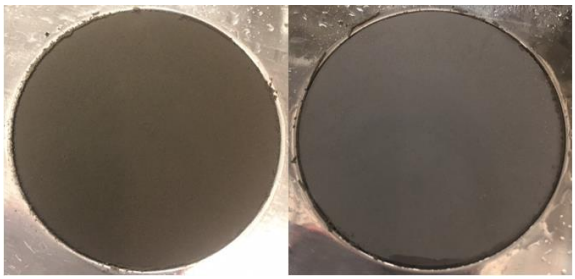

**Figure 13 - Cement (shown left) and steel (shown right) bonded interfaces after testing that show complete bond failure.**

## 5.4. TENSILE BOND STRENGTH

Of the 14 samples originally produced, 11 were successfully prepared and tested. Results from these tests further confirmed the impact of nanoparticles in cement on its bonding potential to a steel substrate. Furthermore, it was continuously observed that at concentrations of 5% BWOC the tensile bond strength of the bond overcame the tensile strength of the cement body which resulted in the tensile failures seen in Figure 14 as opposed to the clean bond failure seen in Figure 9.

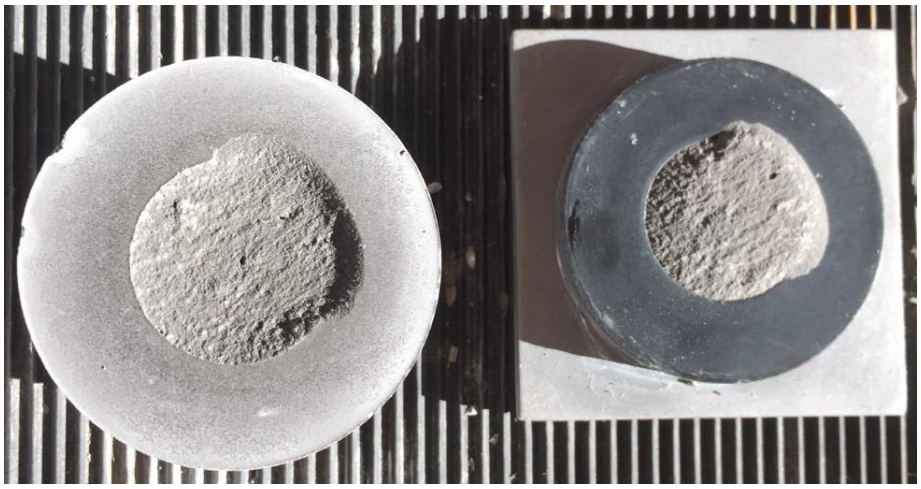

**Figure 14 - Tensile bond strength sample failure within the cement body.**

It was seen in samples that failed as a result of de-bonding, that an increase of the nanoparticle concentration in cement resulted in varying levels of improvement on the strength seen there. Additionally, when samples that failed within the cement body are taken into consideration, a similar trend in the failure load is seen. Table 7 details these results. Please see Table F.10 in appendix F for additional information.

**Table 7 - Summarized tensile bond strength results.**

| | Tensile Load (lbf) | Average Tensile Bond Strength (psi) | Change from Base Case (%) |
|---|---|---|---|
| Base Case | 87 | 114.4 | 0% |
| 1% NP Barite 1 | 103 | Tensile Failure | - |
| 3% NP Barite 1 | 126 | Tensile Failure | - |
| 3% NP Barite | 107.5 | 141.4 | 21% |
| 5% NP Barite 1 | 163.5 | Tensile Failure | - |
| 5% NP Barite 2 | 122.5 | Tensile Failure | - |
| 1% NP Magnetite 1 | 124.5 | 162.5 | 35% |
| 1% NP Magnetite 2 | 100 | 130.5 | 13% |
| 3% NP Magnetite | 108.5 | 141.6 | 21% |
| 5% NP Magnetite 1 | 101 | Tensile Failure | - |
| 5% NP Magnetite 2 | 195.5 | Tensile Failure | - |

## 5.5. YOUNG'S MODULUS

By utilizing the stress strain data obtained in the UCS testing, an evaluation of the Young's Modulus was conducted. ASTM C469 was referenced and slightly altered such that the points used to describe the slope were taken at 35% and 45% of the critical load so that the stiffness was calculated while the sample was still under elastic deformation (see Figure 15).

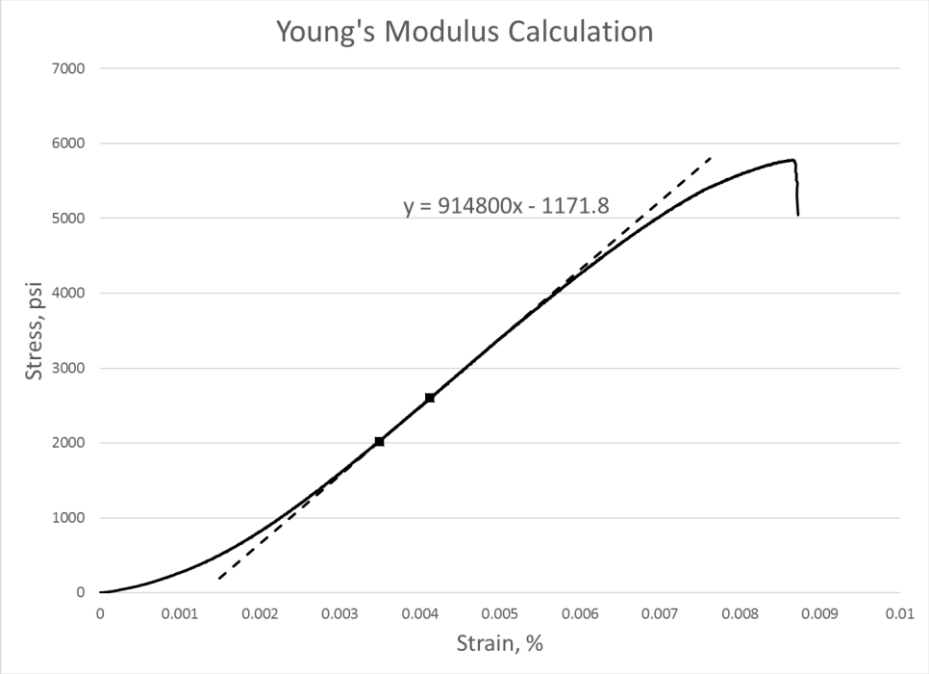


**Figure 15 - Points used to calculate Young's Modulus from stress strain curves.**

Averages for the calculated Young's Modulus values are given in Table 8 and encompass all four UCS samples tested for each case. Overall, the addition of nanoparticles to the base case cement increases the stiffness with their concentration. This however is taken with two notable exceptions; namely the 3% concentrations for both additives, and is detailed in the next section. A detailed accounting of the calculations is available in appendix G and their results are presented in Table F.11 under appendix F.

**Table 8 - Summarized Young's Modulus calculation results.**

| | Mean Young's Modulus (ksi) | CV (%) | Change from Base Case (%) |
|---|---|---|---|
| Base Case | 852.6 | 2.0% | - |
| 1% NP Barite | 862.4 | 2.7% | 1.1% |
| 3% NP Barite | 813.5 | 14.7% | -4.7% |
| 5% NP Barite | 892.9 | 2.1% | 4.6% |
| 1% NP Magnetite | 899.1 | 4.5% | 5.3% |
| 3% NP Magnetite | 813.6 | 12.4% | -4.7% |
| 5% NP Magnetite | 941.0 | 5.3% | 9.9% |

## 5.6. MICROSCOPY

In order to evaluate the microstructure of the cements in question, the Brazilian samples were put to further use as samples for microscopy. After being cut to size and polished with a 3μm diamond suspension, the samples were analyzed visually using scanning electron microscopy (SEM) as well as for bulk composition using energy-dispersive spectroscopy (EDS).

SEM images of the base case samples at 1000x magnification revealed a microporous structure with several distinct features including high density and low density C-S-H represented as points 1 and 2 in Figure 16 and Table 9; as well as a relatively uniform dispersion of micro pores in between the hydrated products. Boundaries between the two C-S-H products were then more clearly defined when analyzing the backscatter images of the same area as shown in Figure 17. Additionally, formations of distinctly bright structures were observed and determined to be largely composed of barium, oxygen, and sulfur. These structures, represented as point 3 in Figure 16 and Table 9, were determined to likely be pockets of consolidated barite.

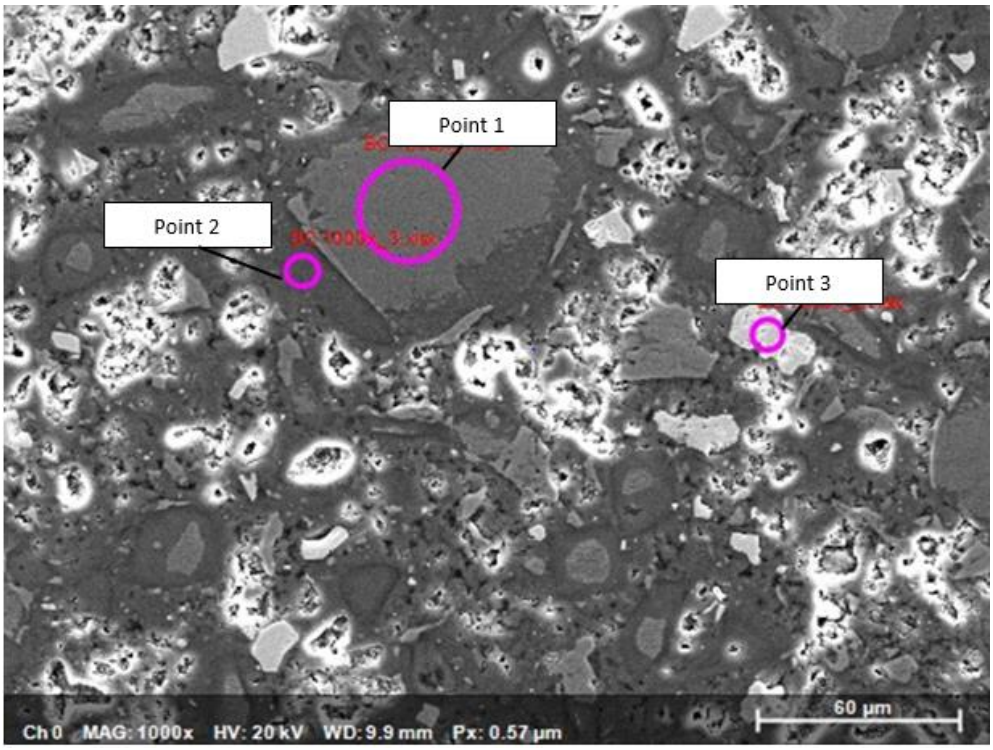


**Figure 16 - Base case SEM image at 1000x.**

**Table 9 - EDS results for a base case sample showing the bulk composition of three points.**

| | Base Case Bulk Composition (%) | | | | | | | |
|---|---|---|---|---|---|---|---|---|
| | Oxygen | Sodium | Aluminum | Silicon | Sulfur | Calcium | Iron | Barium |
| Point 1 | 50.64 | 0.02 | 0.87 | 11.73 | 0.23 | 35.54 | 0.50 | 0.48 |
| Point 2 | 63.98 | 0.07 | 0.87 | 8.69 | 0.47 | 24.91 | 0.91 | 0.10 |
| Point 3 | 63.03 | 0.00 | 0.25 | 2.18 | 13.84 | 7.62 | 0.21 | 12.87 |

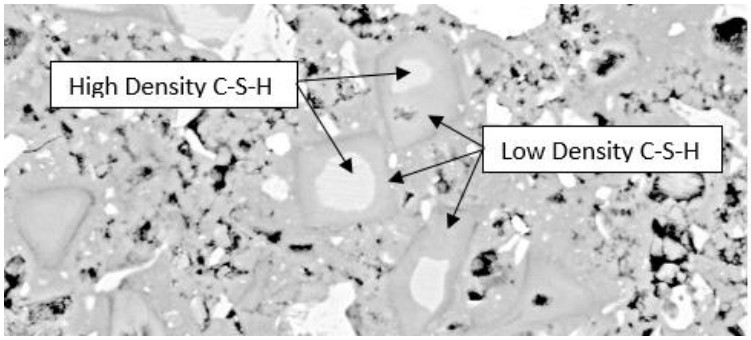


**Figure 17 - Backscatter SEM image at 1000x showing high density and low density C-S-H.**

Similar structures were identified in the 3% nanoparticle barite samples as well as 1%, 3%, and 5% nanoparticle magnetite samples. A full detailing of these results is available in appendix H.

A noticeable change in the frequency of micro pore formation was also observed, particularly in samples containing nanoparticle magnetite. When comparing the SEM images at 1000x magnification of the base case sample and 5% nanoparticle magnetite sample, (Figure 18 and Figure 19 respectively), a distinct reduction in the presence of pores is noticed in between the hydrated cement products.

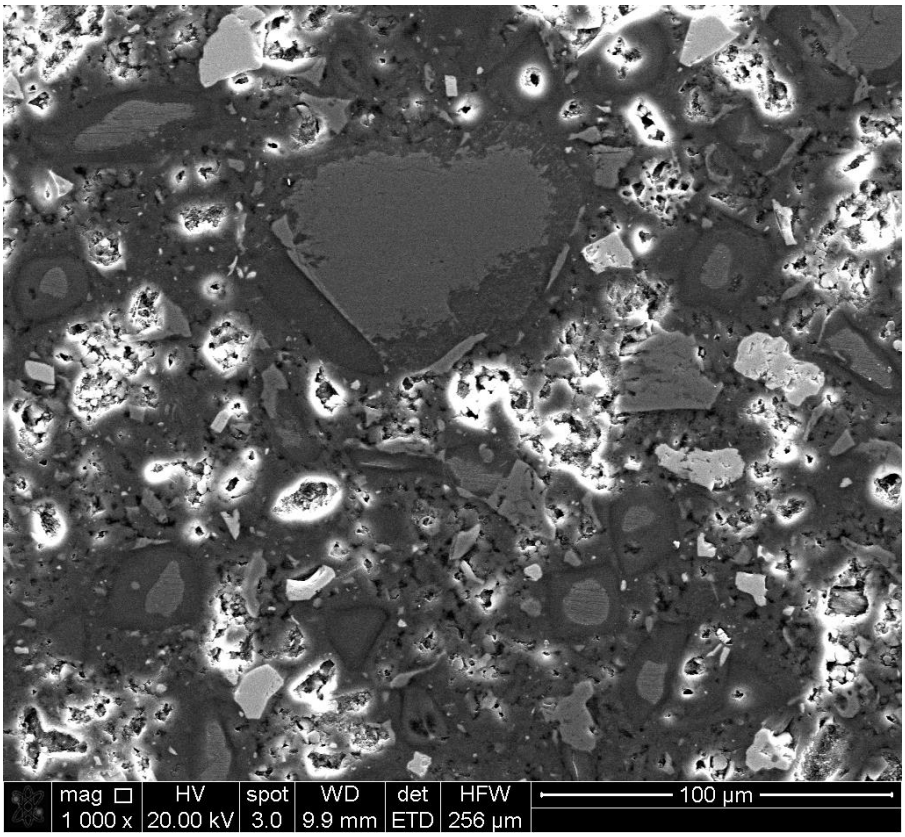


**Figure 18 - SEM image at 1000x magnification of a base case sample.**

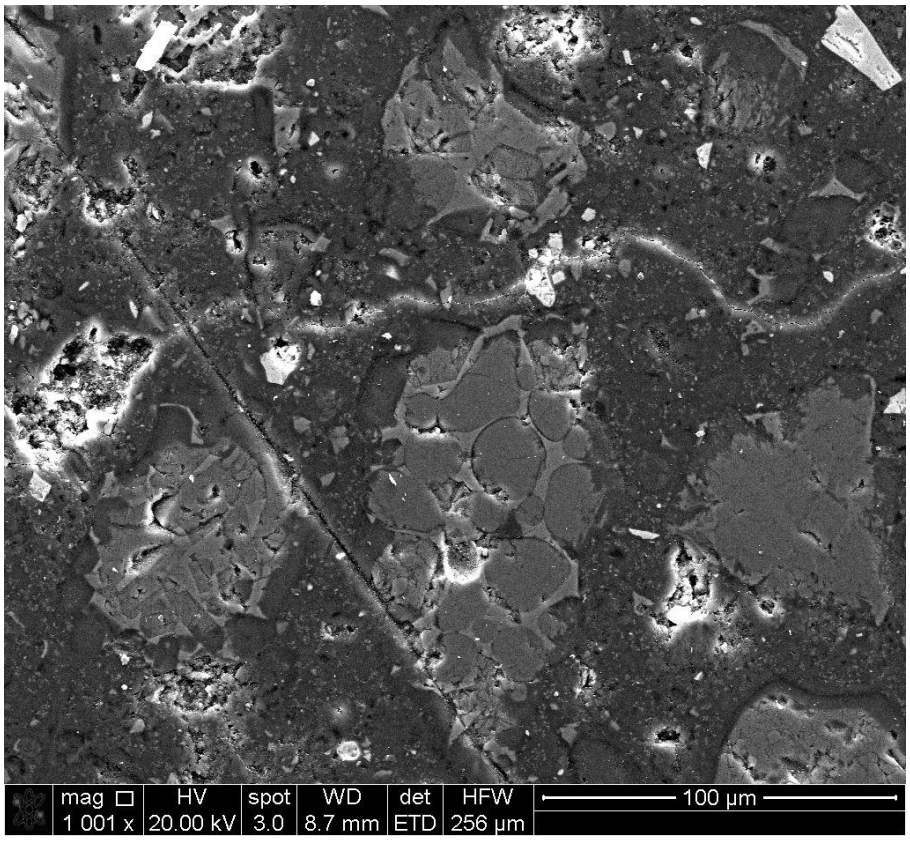


**Figure 19 - SEM image at 1001x of a 5% nanoparticle magnetite sample.**

Further investigation of the backscatter images reveal small points of high density in between the hydration products of samples containing 5% nanoparticle magnetite BWOC shown in Figure 20. These same tiny, high-density points are not seen when looking at the same image of the base case (Figure 21), which leads to the hypothesis that the observed points are in some fashion the added nanoparticles. Whether individual, or in small clusters, the high density points are likely too small to be observed at this magnification alone. For that reason, it is likely that what is being seen is the formation of high density C-S-H that is using the nanoparticles as a nucleation point.

This would not only explain why the high density points are so small but also why they are observed less frequently in samples with less nanoparticles. Such as the case of the 3% BWOC nanoparticle magnetite sample seen in Figure 22.

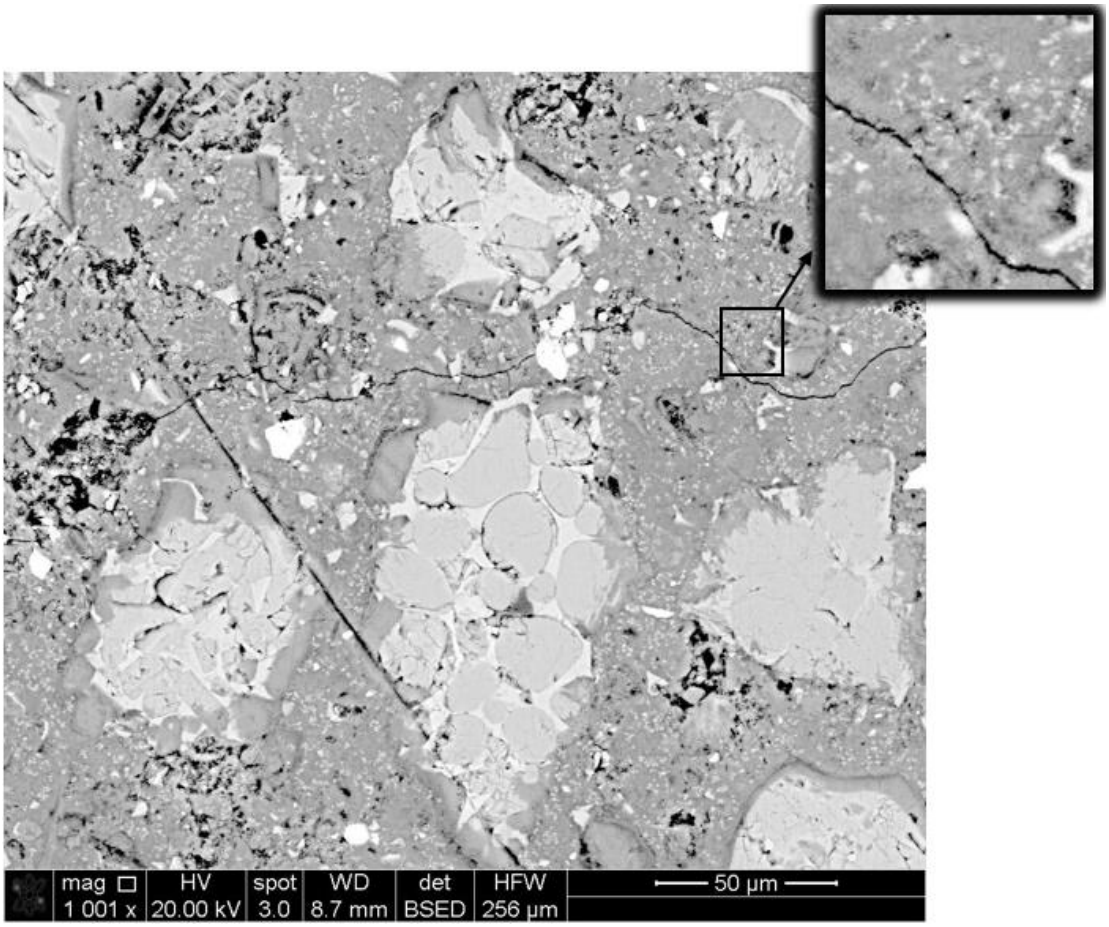


**Figure 20 - Backscatter image of a 5% BWOC nanoparticle magnetite sample with scattered points of high density in between hydration products.**

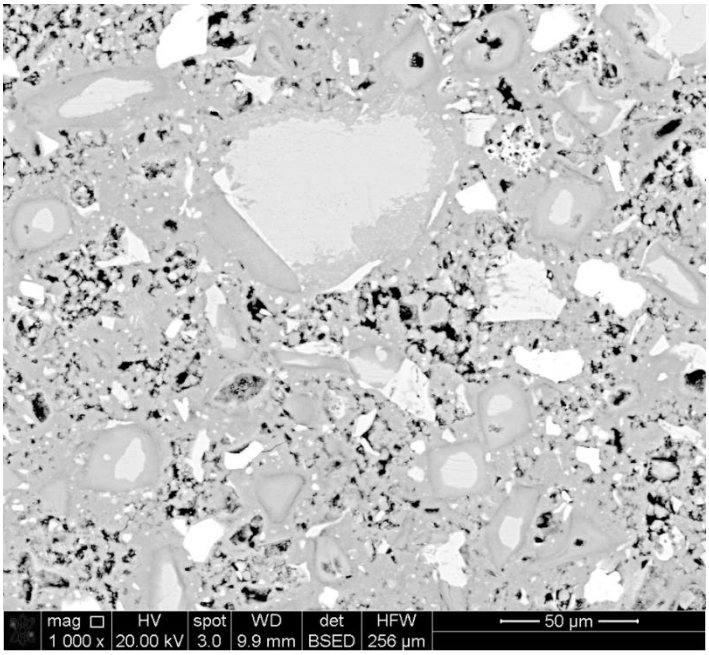


**Figure 21 - Backscattered image of a base case sample.**

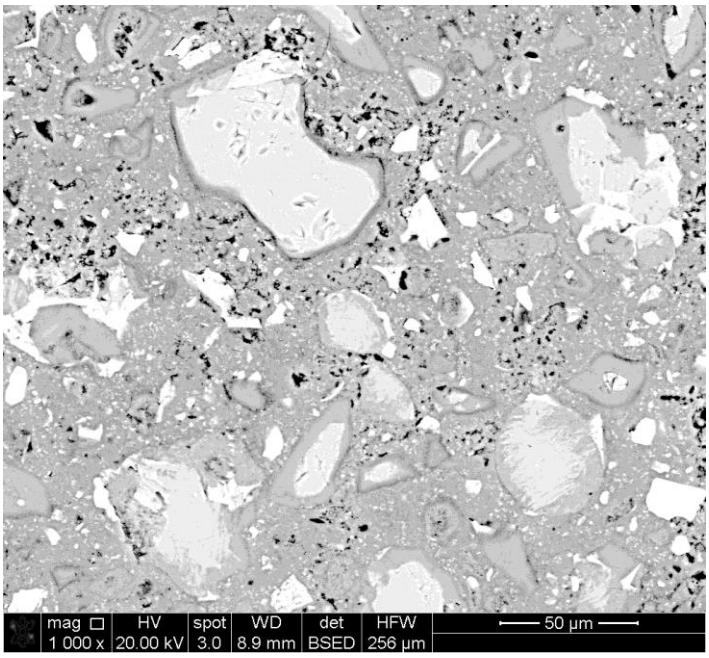


**Figure 22 - Backscatter image of a 3% BWOC nanoparticle magnetite sample.**

At 50,000x magnification the hydration product of the base case sample shown in Figure 23 was seen to develop irregularly and consisted mostly of C-S-H binder with little interaction from additives like standard barite to act as an aggregate. Samples with nanoparticles however, were seen to interact with the C-S-H binder even on the sub micro scale. Figure 24 shows a 5% BWOC nanoparticle barite sample at 50,000x magnification where the dominant feature is a cluster of nanoparticles partially bound together by C-S-H binder. These nanoparticles acted as a substrate for the C-S-H product to form, which in turn provided structure and an added density to the matrix that was not seen in the base case.

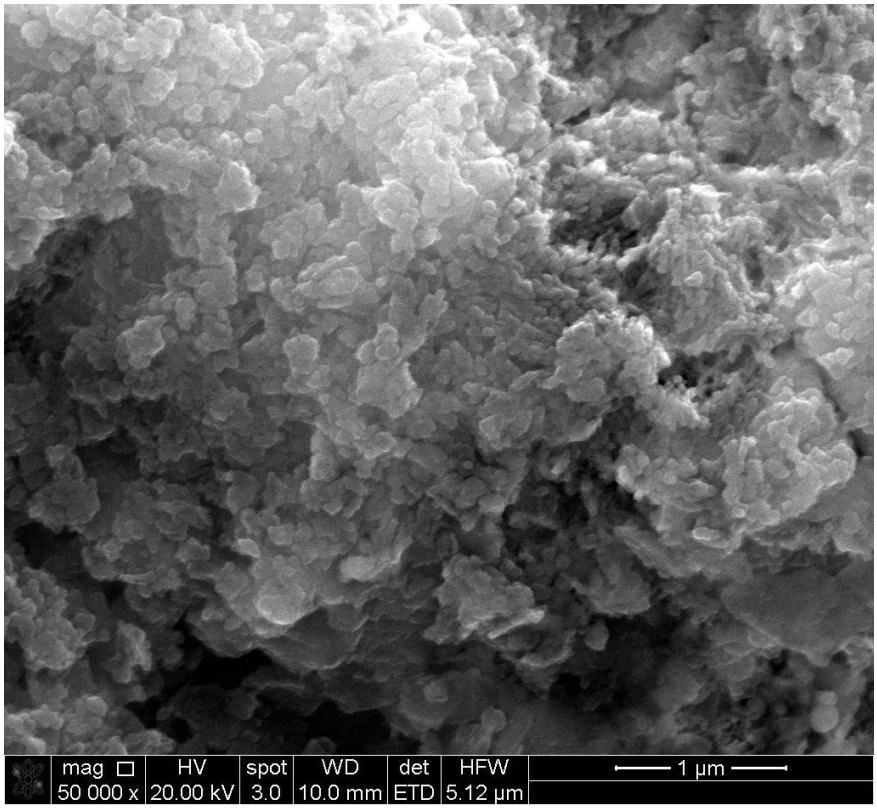


**Figure 23 - SEM image at 50,000x magnification of a base case sample.**

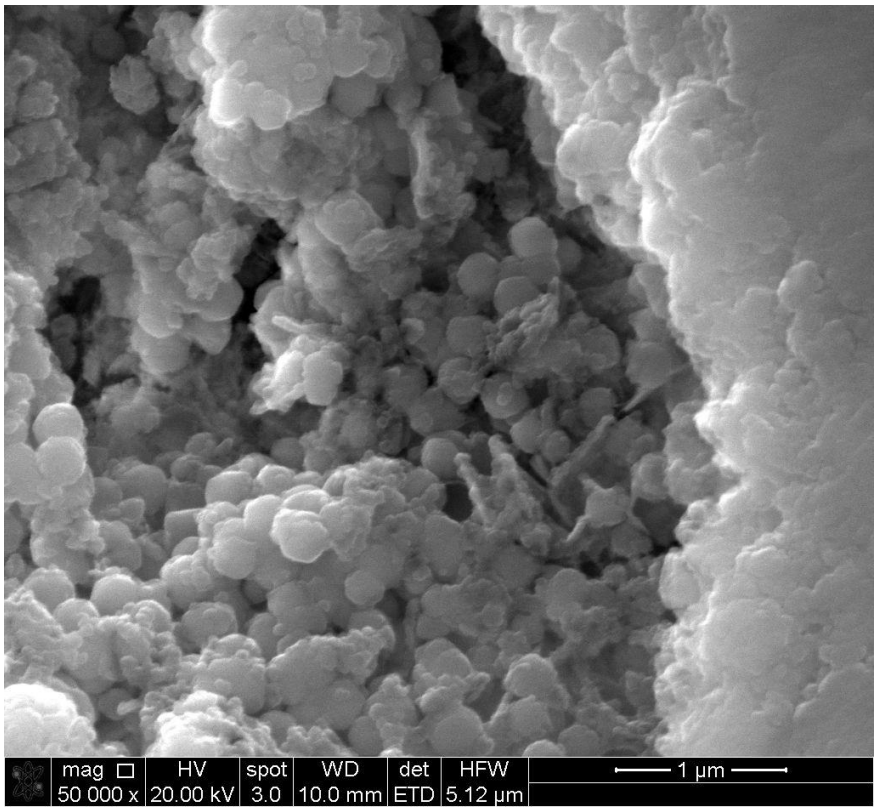


**Figure 24 - SEM image at 50,000x magnification of a 5% BWOC nanoparticle barite sample.**

Furthermore, images of the same samples at 20,000x magnification (shown in Figure 25 and Figure 26) show an increase in the packing efficiency when nanoparticles are present. This resulted in an observable decrease in the presence of crystalline CH due to the volumetric restriction set by the nanoparticle filler.

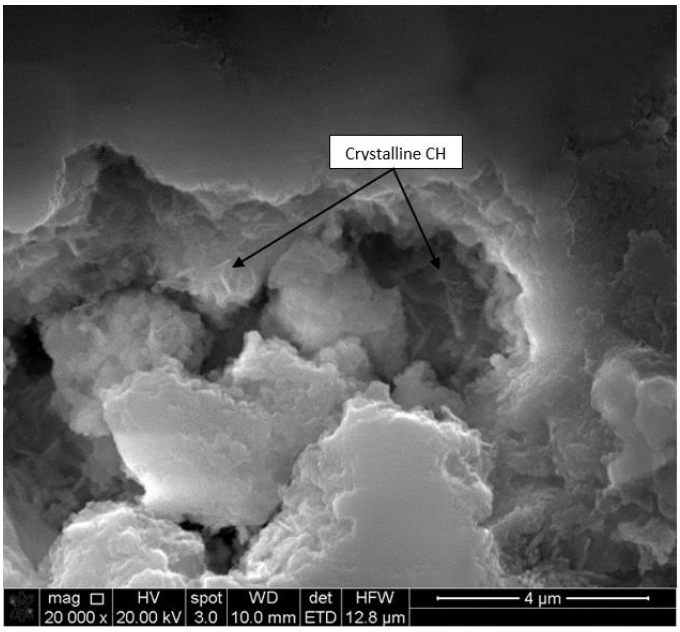


**Figure 25 - SEM image at 20,000x magnification of a base case sample showing crystalline CH formations.**

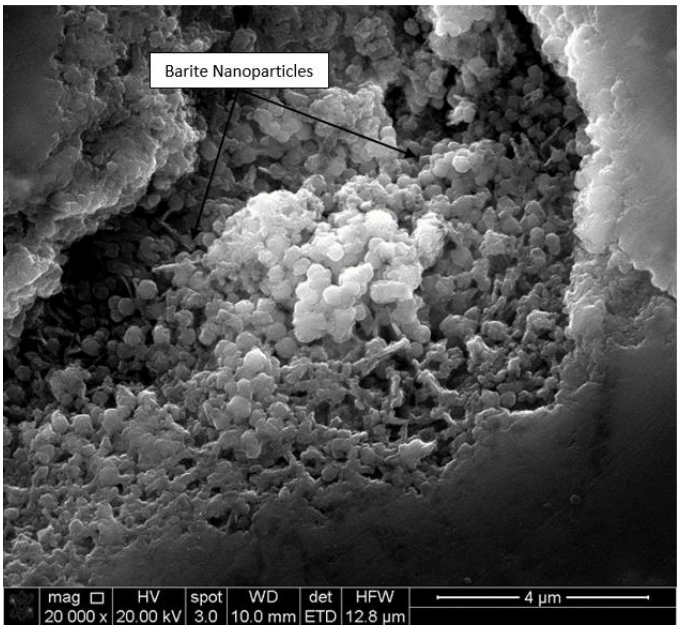


**Figure 26 - SEM image at 20,000 magnification of a 5% BWOC nanoparticle barite sample showing nanoparticles filling void space and restricting CH growth.**

# CHAPTER 6

# DISCUSSION

## 6.1. Cement Strength

Within the cement body, it was seen that the presence of nanoparticles have a positive impact on its compressive strength, and the opposite was seen with regards to the tensile strength. Further investigation into the Young's Modulus of the cement, (detailed in appendix G), revealed that samples containing nanoparticles resulted in higher stiffness values than was seen in the base case with two exceptions.

At concentrations of 3% BWOC, both additives yielded a 4.7% reduction in stiffness when compared to the base case with dramatic increases to their respective variations. Where the coefficients of variation for the other samples ranged between 2-5.3%, the 3% nanoparticle barite and magnetite samples varied 14.7% and 12.4% respectively. This could imply dramatic variations in the packing structure of the hardened cement in each core; caused by the nanoparticles tendency to clump. Additionally, the pockets of barite discussed in section 5.6 describe a scenario involving uneven mixing across the samples that results in pockets of barite that could remain largely unreacted. This would have created weak points within the cement body and explains why such a dramatic decrease in tensile strength was seen against the base case.

Furthermore, when considering the uncharacteristic increase of variation observed in the UCS results for 3% nanoparticle barite samples, two distinct classes of samples are seen. One

slightly higher in compressive strength than the base case, and one significantly lower as illustrated in Figure 27. If unevenly distributed across each of the four cores, it is likely that the presence, (or lack thereof), of nanoparticles is the driving factor behind the observed variation. As was seen in the 5% nanoparticle barite samples, the addition of nanoparticles to cement improves its compressive strength when their concentration within the sample is high enough. Therefore, it is likely that during mixing, the nanoparticles were not uniformly distributed throughout the slurry and as such, sample numbers 2 and 3 of the 3% nanoparticle barite set saw increased compressive strength. Additionally, it can be further speculated that the dramatic reduction in compressive strength seen in samples 1 and 4 was a symptom of the nanoparticles extremely high surface area to volume ratio.

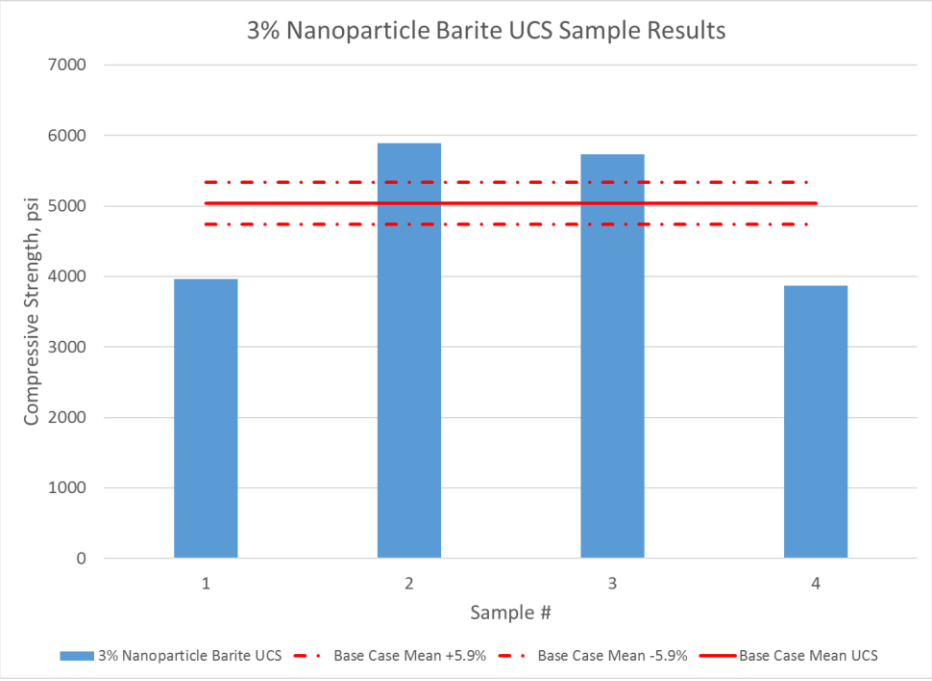


**Figure 27 - 3% nanoparticle barite BWOC sample UCS results compared to the average base case with variation considered.**

As discussed in section 3.1.1, it was seen that nanoparticle barite required more water to fully wet its surface than standard barite by nearly a factor of nearly 10. That is because the surface energy of nanoparticles have stronger hydrophilic tendencies; and their large surface area to volume ratio means that a larger proportion water is temporarily bound to each particle than is to their larger counterparts. This fact, coupled with the clumping behavior of nanoparticles, means that when nanoparticles are not uniformly distributed within the slurry the water will also disproportionately be found with them in the setting cement. In turn, less water available for reaction throughout the cement will then lead to unreacted and partially reacted zones with less C-S-H product formation that dramatically weakens the cement.

## 6.2. Cement/Steel Bonding

Within the transition zone between cement and the steel substrate, an overall increase in strength of the bond created there was observed. To an extent, this improvement in bonding strength was seen in both cases of nanoparticle additives which implies that the size of the particle has an impact on the cements interaction with steel. As previously mentioned, the various products of cement hydration have varying adhesive strengths when in contact with steel, (Li et al., 2018). CH has been seen to form large, irregularly shaped crystals that are poorly suited to bonding with steel; while the remaining hydration products have a stronger affinity for it. Therefore minimizing their presence in favor of high and low density C-S-H, as well as unreacted and various miscellaneous phases increase the potential strength at such a material interface.

Another side effect of nanoparticles holding large amounts of water is the fact that they then become nucleation sites for the hydration reaction as was seen in Figure 24. On their surface,

the nanoparticles provide a point for water to react and form CH gel which is then consumed and refined to create the various C-S-H products (Horszczaruk, 2019; Li et al., 2004; Khoshakhlagh, Nazari and Khalaj, 2012; Soltanian et al., 2015). Therefore, nanoparticles in the cement slurry both increase the packing efficiency of the set cement by filling nano-sized voids in between the standard particles while reducing the size and presence of CH crystals. This reaction based on the particle size then makes the overall cement body better equipped to bonding with exterior substrates.

Magnetite nanoparticles are known to naturally have magnetic properties, (Xu et al., 2007), and as such it has been theorized that they could provide an even stronger bond to a ferritic substrate such as standard steel. While present, the magnetism itself is not likely to be strong enough to benefit the bond, however, it could draw larger concentrations of the nanoparticles in the local vicinity closer to its surface. This would then further reduce the CH presence in this zone and increase the bond strength seen there, which could explain why the bond strength seen with nanoparticle magnetite was larger than that seen by nanoparticle barite.

Tensile bond strength of the cement samples increased with the presence of nanoparticles until the ultimate strength of the bond surpassed the ultimate tensile strength of the cement. It has been noted that the presence of nanoparticles in the set cement reduces the ultimate tensile strength of the cement body, however, when comparing the load at failure across the tested samples a similar positive trend is seen as shown in Figure 28. This indicates that with nanoparticles present within the cement, the point of concern is no longer at the material interface, but within the cement body itself.

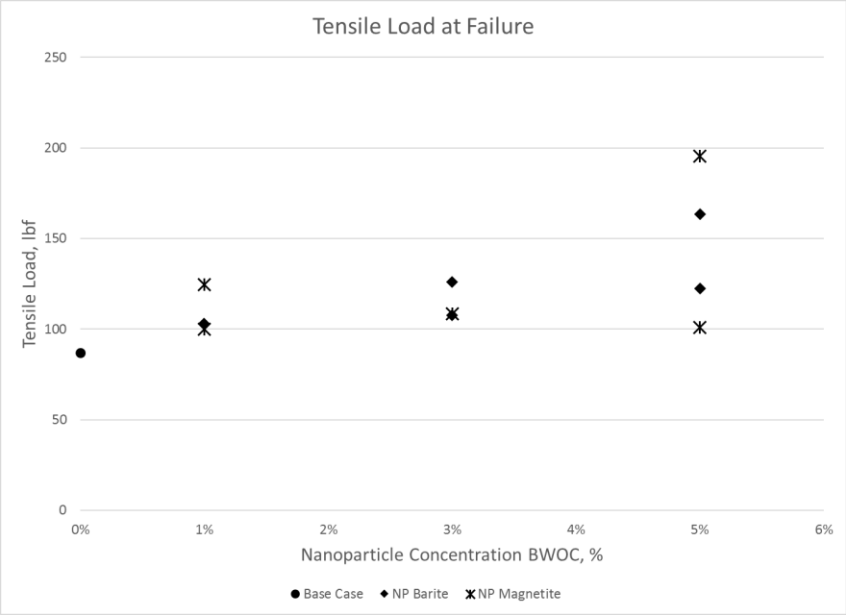


**Figure 28 - Tensile load at failure for all tensile bond strength samples tested, regardless of failure mechanism.**

# CHAPTER 7

# CONCLUSION

In this study, the mechanical behavior of two nanoparticle additives were evaluated when acting as weight replacements in a heavy, class H, field ready cement. Standard procedures were used to analyze the compressive as well as tensile strength, and two new or modified experiments were established to evaluate the cement bond strength to a steel substrate in both the shear and direct tensile modes of failure. The effects observed are as follows:

- Nanoparticle barite yielded marginal changes to the compressive strength where at 5% BWOC a 7.6% improvement was seen. Nanoparticle magnetite resulted in a wide range of improvement where concentrations of 1%, 3%, and 5% BWOC were observed to increase the compressive strength 20.5%, 8.9%, and 19.2% respectively.
- By analyzing the Young's Modulus (stiffness), variations in the hardened cement structure were seen. This is likely due to variations in the nanoparticle concentration between samples of the same sample recipe due to clumping and water dispersion. The effects of which would be seen throughout all of the samples discussed in this thesis.

- The tensile strength was seen to decrease with the addition of nanoparticles as a result of the increased stiffness coupled with the discontinuous matrix of cement hydration products and unreacted material in the cement body. While the nanoparticles worked to increase the stiffness of the reacted cement, the pockets of unreacted material reduced the effective area of the cement binder product. This reduced the portion of the cement matrix that could support a load, and therefore reduced the tensile strength of the cement body overall.
- Shear bond strength between the set cement and a steel substrate was seen to increase with the concentration of nanoparticles in the cement. This is likely a result of the nanoparticles reducing the production of CH crystals near the material interface, which in turn increased the surface area bonded to the steel.
- Tensile bond strength was observed to increase with nanoparticle concentration until overcoming the tensile strength of the cement body. The failure loads from these tests described a scenario where the bond strength at the material interface is no longer the likely failure point when under tensile loading.
- It was seen in the microscopy results that across all of the samples, clumping and uneven mixing occurred to some degree. While in practice variance in composition across the cement body is to be expected; these unreacted and partially reacted pockets of additives create discontinuities in the binding matrix therefore weakening the overall structure. A great deal of strength could be added to cement by simply ensuring a uniform mixture.

Results of this study show an increase in compressive strength as well as potential bond strength as the concentration of nanoparticles increases. This suggests that during well operations with decreased casing pressure, the likelihood of a micro-annulus forming in between the cement

and casing is significantly reduced. Furthermore, a reduction in tensile strength is observed as a result of an increased stiffness of the cement body as well as uneven distribution of nonreactive additives and water. Sonication of the nanoparticles suspended in the mix water could aid in fixing this issue for lab purposes, while an effective dispersant could be utilized for field applications.

If implemented correctly, nanoparticles used as weight replacement additives could mitigate the risk of micro-annuli formation at the casing-cement contact. Thereby creating a more robust seal between the reservoir and environment for both primary as well as plug and abandon cementing operations.

# REFERENCES


Alkhamis, M., & Imqam, A. (2018). New Cement Formulations Utilizing Graphene Nano Platelets to Improve Cement Properties and Long-Term Reliability in Oil Wells. Society of Petroleum Engineers. doi:10.2118/192342-MS

Bolhassani, M., & Sayyahmanesh, M. (2015). A study on mechanical properties of cement paste using magnetite-silica nano-composites. Advances in Cement Research, 27(10), pp.571-580.

Camiletti, J., Soliman, A.M. & Nehdi, M.L.(2013). Effects of nano- and micro-limestone addition on early-age properties of ultra-high-performance concrete. Materials and Structures Vol. 46: 881. https://doi.org/10.1617/s11527-012-9940-0

Carter, L. and Evans, G. (1964). A Study of Cement-Pipe Bonding. Journal of Petroleum Technology, 16(02), pp.157-160.

Douba, A., Genedy, M., Matteo, E., Kandil, U., Stormont, J., & Taha, M.R. (2017). The Significance of Nanoparticles on Bond Strength of Polymer Concrete to Steel. International Journal of Adhesion and Adhesives. 74. 10.1016/j.ijadhadh.2017.01.001.

El-Gamal, S.M.A., Abo-El-Enein, S.A., & El-Hosiny, F.I. et al. (2015). Fe2O3 nanoparticles improve the physical properties of heavy-weight wellbore cements: A laboratory study. Journal of Natural Gas Science and Engineering 26. https://doi.org/10.1007/s10973-017-6629-1

García, V., Márquez, C., Zúñiga-Suárez, A., Zuñiga-Torres, B. & Villalta-Granda, L. (2017). Brazilian Test of Concrete Specimens Subjected to Different Loading Geometries: Review and New Insights. International Journal of Concrete Structures and Materials, 11(2), pp.343-363.

Guo H., Aziz N.I., & Schmidt L.C., (1992). Rock Fracture-Toughness Determination by the Brazilian Test. BHP Iron Ore Ltd, Newman, W.A., Australia University of Wollongong, Wollongong, N.S.W., Australia

Heinold, T., Dillenbeck, R. L., & Rogers, M. J. (2002). The Effect of Key Cement Additives on the Mechanical Properties of Normal Density Oil and Gas Well Cement Systems. Society of Petroleum Engineers. doi:10.2118/77867-MS

Iremonger, S. S., Bolt, M., & Lawrence, S. C. (2015). Enhanced Thermal Well Integrity Through The Use Of A New Cement Tensile Strength-enhancing Fiber. Society of Petroleum Engineers. doi:10.2118/174483-MS

Jafariesfad, N., Geiker, M., Gong, Y., Skalle, P., Zhang, Z. & He, J. (2017). Cement sheath modification using nanomaterials for long-term zonal isolation of oil wells: Review. Journal of Petroleum Science and Engineering, 156, pp.662-672.

Jaishankar, P., &Mohan, K.S.R. (2015). Experimental investigation on Nano particles in High Performance Concrete. International Journal of Chemical Technology Res.1666–1670.

Jasiczak, J., Kulczewski, P., & Borowski, P. (2017). Laboratory Tests of Adhesion of Steel Bars to Ordinary and Frozen Concrete. IOP Conference Series: Materials Science And Engineering, 245, 032043. doi: 10.1088/1757-899x/245/3/032043

Jimenez, W. C., Urdaneta, J. A., Pang, X., Garzon, J. R., Nucci, G., & Arias, H. (2016). Innovation of Annular Sealants During the Past Decades and Their Direct Relationship with On/Offshore Wellbore Economics. Society of Petroleum Engineers. doi:10.2118/180041-MS

Jo, B., Kim, C., Tae, G. & Park, J. (2007). Characteristics of cement mortar with nano-SiO2 particles. Construction and Building Materials, 21(6), pp.1351-1355.

Khoshakhlagh, A., Nazari, A. & Khalaj, G. (2012). Effects of Fe2O3 Nanoparticles on Water Permeability and Strength Assessments of High Strength Self-Compacting Concrete. Journal of Materials Science & Technology, 28(1), pp.73-82.

Li, H., Xiao, H., Yuan, J. & Ou, J. (2004). Microstructure of cement mortar with nano-particles. Composites Part B: Engineering, 35(2), pp.185-189.

Li, H., Du, T., Xiao, H., & Zhang, Q. (2017). Crystallization of calcium silicate hydrates on the surface of nanomaterials. American Ceramic Society.

Li, Y., Yang, J. & Tan, T. (2018). Measuring adhesion between steel and early-hydrated Portland cement using particle probe scanning force microscopy. Cement and Concrete Composites, 90, pp.126-135.

Liu, X., Chen, L., Liu, A., Wang, X. (2012). Effect of Nano-CaCO3 on Properties of Cement Paste. Energy Procedia, 16, pp.991-996.

McDaniel, J., Watters, L., & Shadravan, A. (2014). Cement Sheath Durability: Increasing Cement Sheath Integrity to Reduce Gas Migration in the Marcellus Shale Play. Society of Petroleum Engineers. doi:10.2118/168650-MS

Najigivi, A., Khaloo, A., Iraji zad, A. & Abdul Rashid, S. (2013). Investigating the effects of using different types of SiO2 nanoparticles on the mechanical properties of binary blended concrete. Composites Part B: Engineering, 54, pp.52-58.

Nazari, A., & Riahi, S. (2012). The effects of ZnO2 nanoparticles on split tensile strength of self-compacting concrete, Journal of Experimental Nanoscience, 7:5, 491-512, DOI: 10.1080/17458080.2010.524669

Nelson, E. B. & Guillot, D. (eds.) 2006. Well cementing, 2nd edition. Amsterdam: Schlumberger.

Shekari, A. & Razzaghi, M. (2011). Influence of Nano Particles on Durability and Mechanical Properties of High Performance Concrete. Procedia Engineering, 14, pp.3036-3041.

Sikora, P., Cendrowski, K., Horszczaruk, E. & Mijowska, E. (2018). The effects of Fe 3 O 4 and Fe 3 O 4 /SiO 2 nanoparticles on the mechanical properties of cement mortars exposed to elevated temperatures. Construction and Building Materials, 182, pp.441-450.

Talabani, S., Chukwu, G. A., & Hatzignatiou, D. G. (1993). Gas Channeling and Micro-Fractures in Cemented Annulus. Society of Petroleum Engineers. doi:10.2118/26068-MS

Thiercelin, M. J., Dargaud, B., Baret, J. F., & Rodriguez, W. J. (1997). Cement Design Based on Cement Mechanical Response. Society of Petroleum Engineers. doi:10.2118/38598-MS

Wilson, D. C., Eustes, A. W., & Fleckenstein, W. W. (2018). Lab Testing Cement-Steel Bonding at Shallow Temperature and Pressure Conditions. Society of Petroleum Engineers. doi:10.2118/190031-MS

Xu, J., Yang, H., Fu, W., Du, K., Sui, Y., & Chen, J. et al. (2007). Preparation and magnetic properties of magnetite nanoparticles by sol–gel method. Journal Of Magnetism And Magnetic Materials, 309(2), 307-311. doi: 10.1016/j.jmmm.2006.07.037

Zhang, Z., Scherer, G.W., & Prud'Homme, R.K. (2016). Adhesion and Bonding Between Steel Pipe and Cement/Spacer/Mud System. 9th International Conference on Fracture Mechanics of Concrete and Concrete Structures doi:10.21012/FC9.313

# APPENDICES

## Appendix A

Appendix A outlines the procedure used to determine the water requirements for samples of cement additives known as the 'Vortex Method'.

Ambient air has varying degrees of humidity that changes based on any number of conditions. This causes partial hydration of cement and its various additives depending on its exposure to it. Because of this fact, the recommended water requirements for any cement component can be changed and need to be verified before testing can begin.

For this study the procedure commonly known as the 'Vortex Method' was used to verify water requirements. This procedure evaluates the saturation of the component in question to a fixed amount of water and qualitatively determines when peak saturation occurs by using the following steps:

1. 200 grams of mix water (simulated sea water in this case) is measured into a mixing cup.
2. An amount of material slightly less than that of the recommended water requirements is measured and added to the mixing cup.
3. The mixer is then set to 4000 RPM and allowed to mix until a uniform slurry is formed.
4. The circular opening of the vortex that forms is then observed and its size approximated.

5. If the opening is not consistently formed or is larger than 1cm, more material should be added until it reaches 1cm in diameter.
    a. If the opening is smaller than 1cm, the slurry should be discarded and steps 1-4 should be done again.
6. Once the vortex opening is observed to be approximately 1cm in diameter, the water requirements are then calculated by dividing the 200 grams of water by the total mass of the material added.

## Appendix B

Appendix B briefly outlines the porosity issues described in section 3.1.1 and details solution.

Testing of the nanoparticle barite sample set revealed the possibility that the higher water requirements initially assumed to be required by the nanoparticle barite, could possibly be detrimental to the cement's strength. The trend established showed that the tensile strength of the cement was inversely related to the concentration of the nanoparticle barite, however the observed porosity increased with the concentration. Excess water coating the nanoparticle surfaces created large pockets of water when the nanoparticles clumped together. These pockets of water remained largely unreacted and are likely the cause of the increase in porosity. Additionally, post failure analysis of the samples revealed that some of the larger pores appeared to have a white coating similar in color to the nanoparticle barite on the pore walls (Figure B. 1). This theory was tested by simply making cores of 5% nanoparticle barite BWOC samples similar to those tested, with the only change being the water requirements for the nanoparticle barite was reduced to that of standard barite and comparing them to a full core of the original recipe. The porosity was observed to be drastically decreased though not all together absent as shown in Figure B. 3 when compared with Figure B. 2. This means that while a considerable amount of the pores were created by the mechanism described above, it is likely that pockets of trapped air within the sample were still present and future samples will need to be stirred to remove the remaining voids.

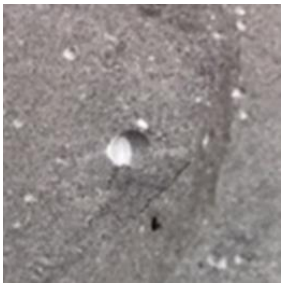

**Figure B. 1 - Closed up image of pore in a nanoparticle barite sample.**

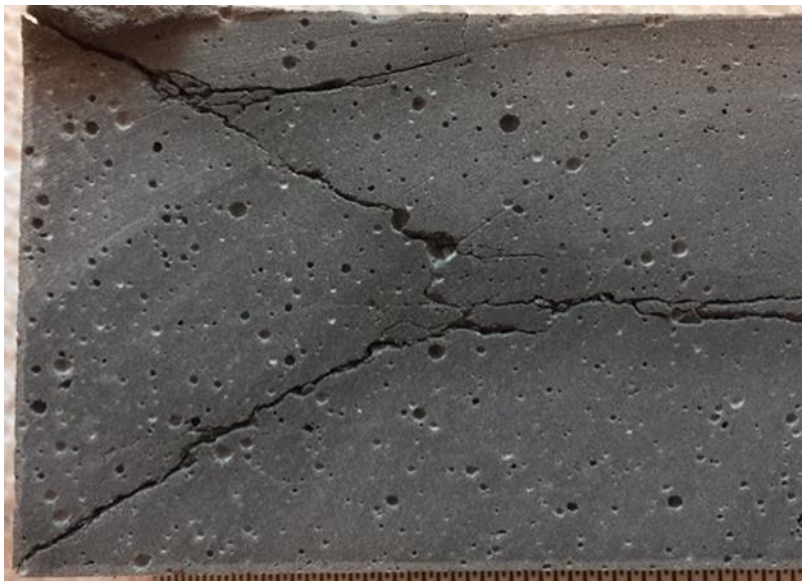

**Figure B. 2 - Cross section of a 5% BWOC nanoparticle barite core after UCS testing that shows highly porous structure.**

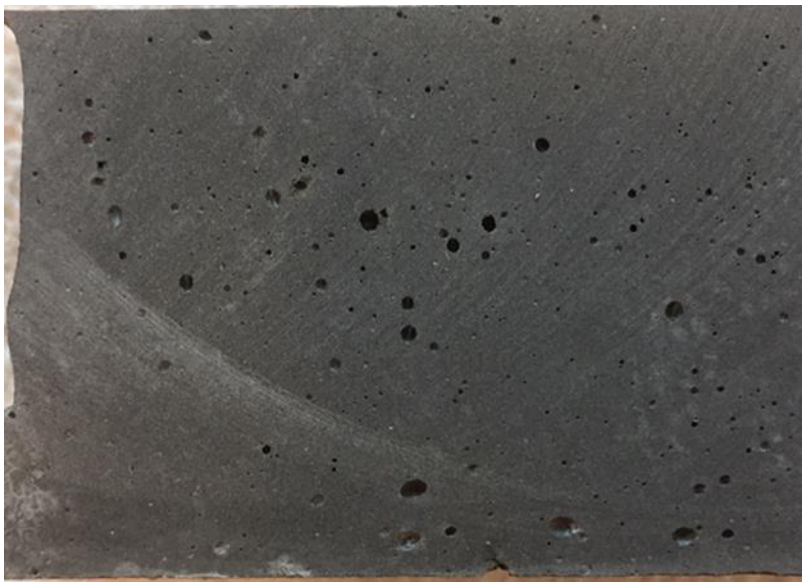

**Figure B. 3 - Cross section of a 5% BWOC nanoparticle barite core with defoamer used that shows a reduction in pore frequency.**

## Appendix C

Appendix C briefly describes and provides diagrams of the curved platens used in the Brazilian tensile testing.

In an effort to provide the ideal loading conditions for the Brazilian testing for tensile strength of the cement samples, a curved platen was used to provide loading to the sample. These platens were designed such that the loading was uniform and applied parallel to the movement of the crossheads. The contact area of the platens were curved to match an arc length equal to a subtended angle of 12° of the 2 inch diameter cement disks (Garcia, et al., 2017). Furthermore, the curvature along the contact surface of the platens was inverted beyond the point marking 12° so that the load was gradually dissipated as the angle increased; as opposed to a corner that could potentially cause a high stress point. This apparatus is further detailed in Figure C. 1.

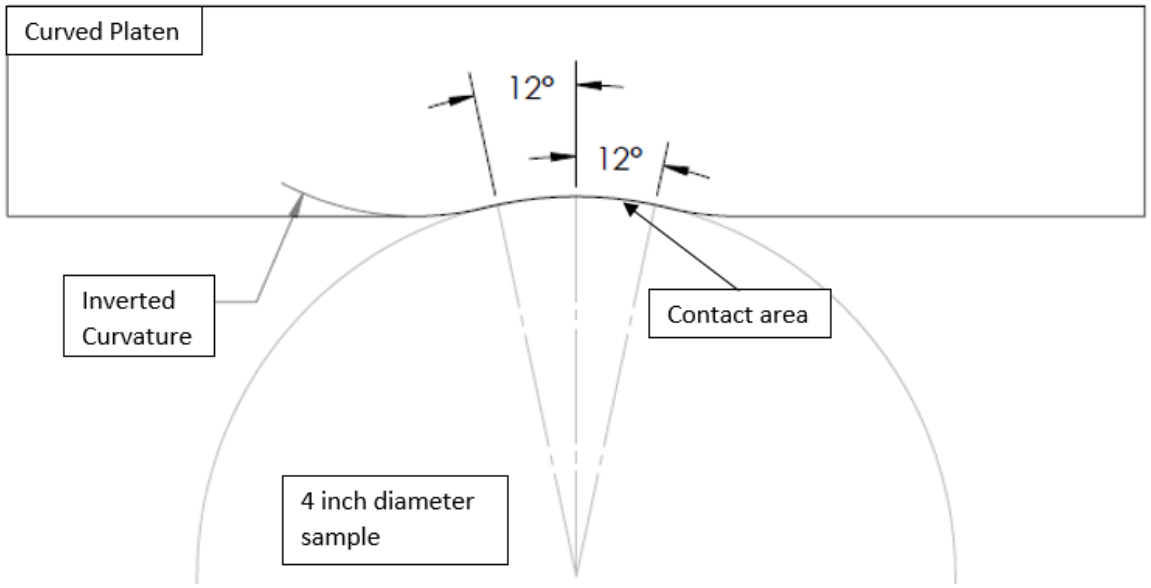


**Figure C. 1 - Detailed sketch of new Brazilian test curved platens at the contact point with a sample.**

## Appendix D

Appendix D details the design and function of the shear bond testing apparatus that was fabricated for, and used in this study.

Drawing from the setup used in Zhang's 2016 study, the shear bond strength between cement and steel was evaluated using a testing apparatus that resembles the split core test. Two halves of an aluminum alloy 6061 cylinder make up the main body of the sample holder that are able to freely slide past each other along the induced failure plane they create. One side contains a centrally placed, 2 inch diameter hole that houses the cement side of the sample puck and therefore applies the shearing load to the sample. The other side has a matching hole, whose depth matches the thickness of the steel coin substrates used for testing to the nearest $5/1000^{th}$ of an inch. This side acts as the support for samples during load testing and as a means of aligning the cement/steel transition zone of the sample to the failure plane of the sample holder.

In order to confidently test at the desired angle across multiple samples, flat edges were milled along the length of the complete cylinder tangent to the arc from which they were cut. Parallel faces were milled diametrically opposite of the first and together correspond to form loading angles that are 15°, 30°, and 45° away from the induced failure plane. This means that the set up is able to reliably test the shear bond strength at angles of 45°, 60°, and 75° from the horizontal. Please see Figure D. 1, Figure D. 2, Figure D. 3, Figure D. 4, Figure D. 5, and Figure D. 6 for detailed sketches of the setup.

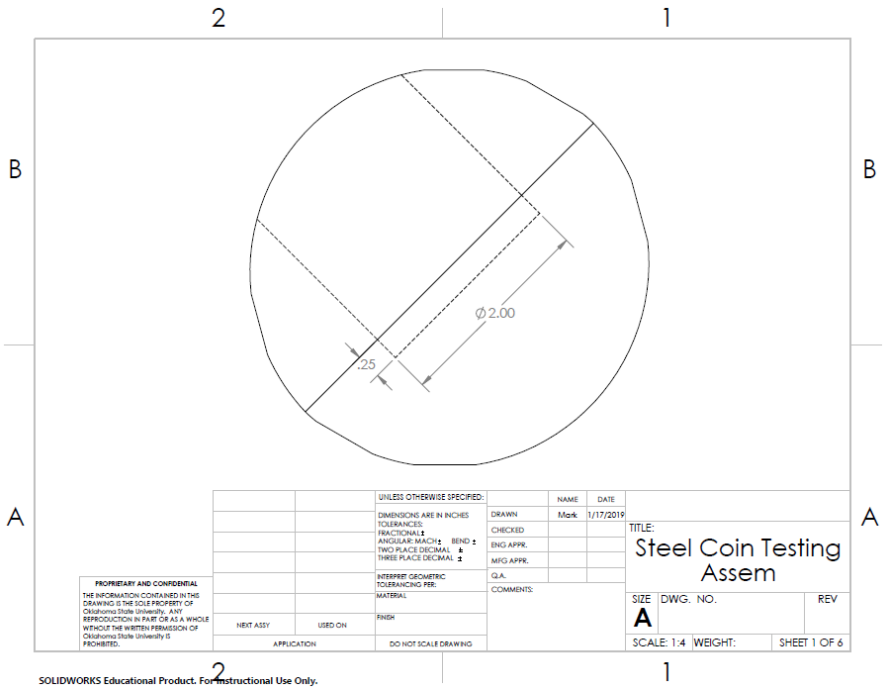


**Figure D. 1 - Dimensions of shear bond test sample holder.**

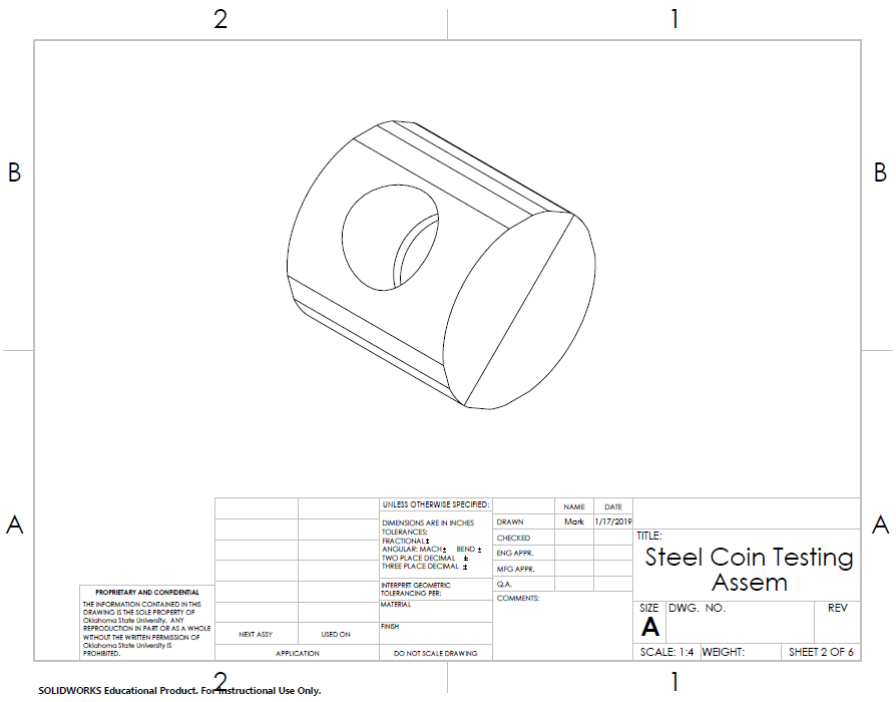


**Figure D. 2 – Visualization of shear bond test sample holder.**

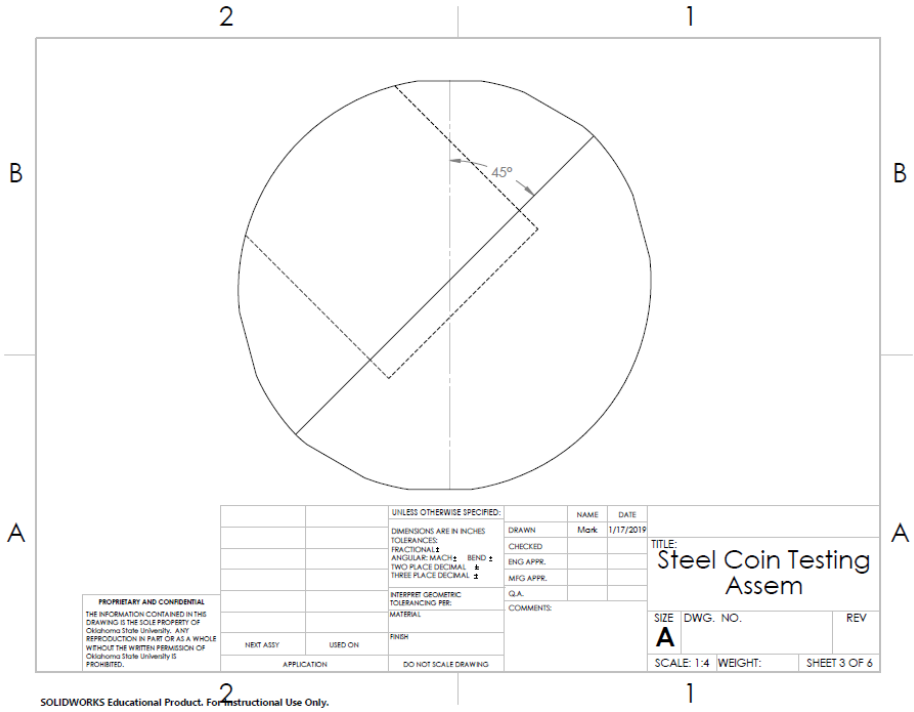


**Figure D. 3 - Shear bond test sample holder at 45° from horizontal.**

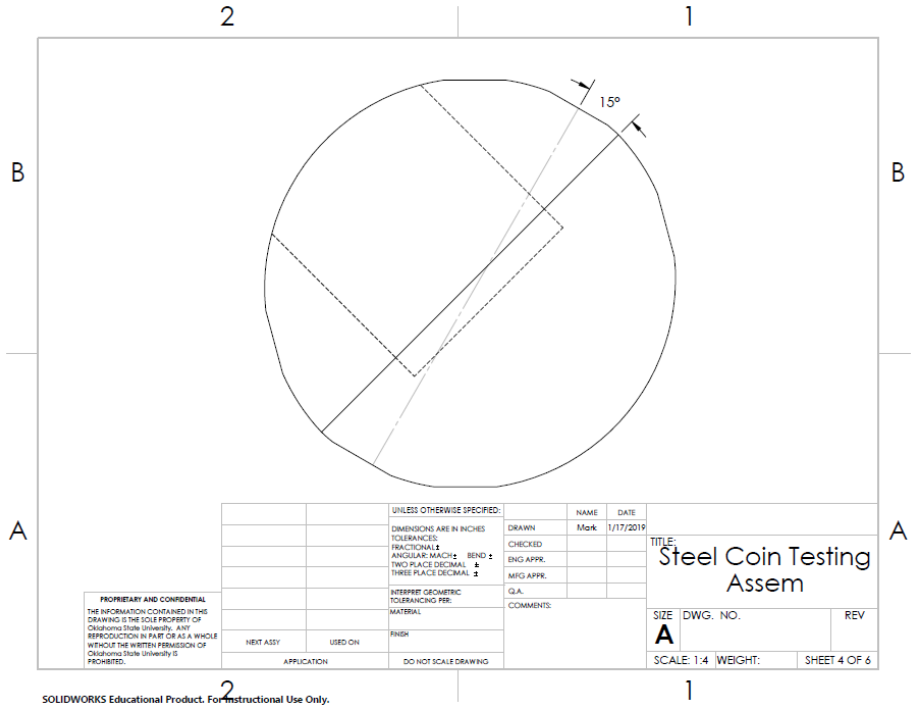


**Figure D. 4 - Shear bond test sample holder noting the 75° platen.**

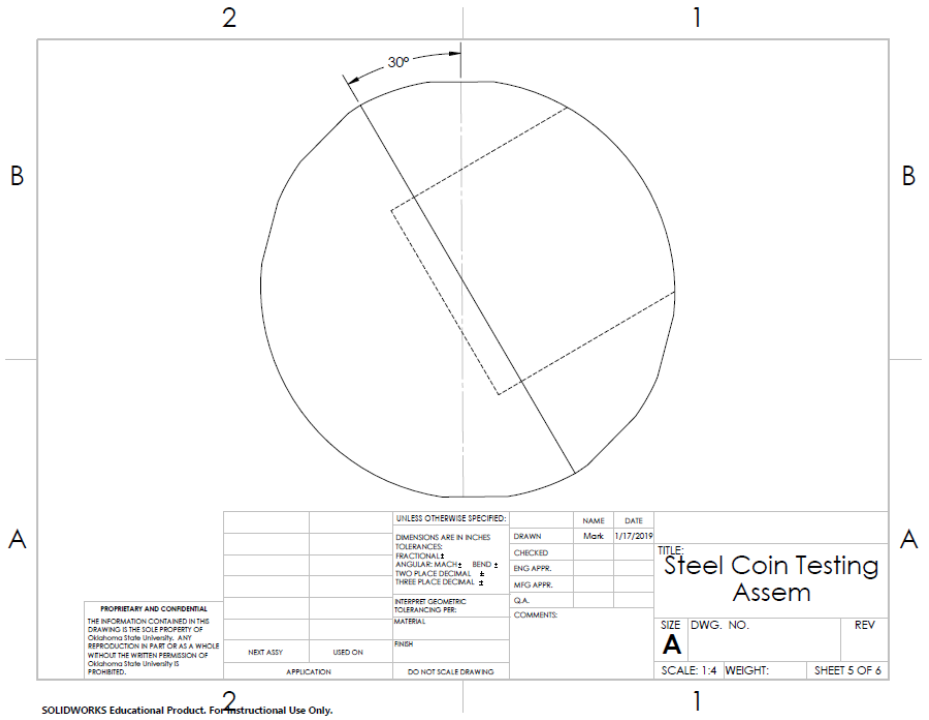


**Figure D. 5 - Shear bond test sample holder at 60° from the horizontal.**

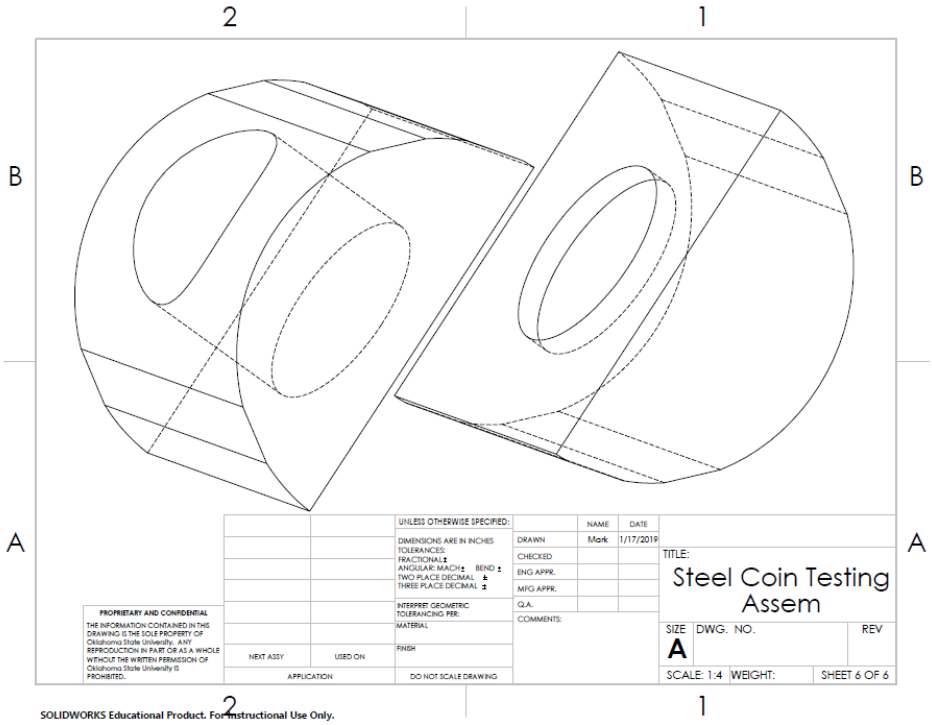


**Figure D. 6 - Exploded view of shear bond test sample holder.**

In order to verify that the aluminum selected to fabricate the sample holder halves can are safe to use, load simulations were ran using the design program Solidworks. These models used the properties of 6061 alloy aluminum to match the aluminum used to fabricate the sample holders, as well as a 2 inch cylinder in place of the cement/steel puck that would be there in testing. This 2 inch cylinder was modeled to have the properties of plain carbon steel so that it would act as a hard inclusion for simulation purposes. The model was bound such that the steel cylinder was in full contact with the sample holder halves; the interacting plane between the sample holder halves was fixed as a roller so that only lateral movement parallel to the planes was allowed and assumed frictionless; the loaded platen had an external load applied; and the platen opposite of the loaded side was fully fixed to act as a base. This is further illustrated in Figure D. 7.

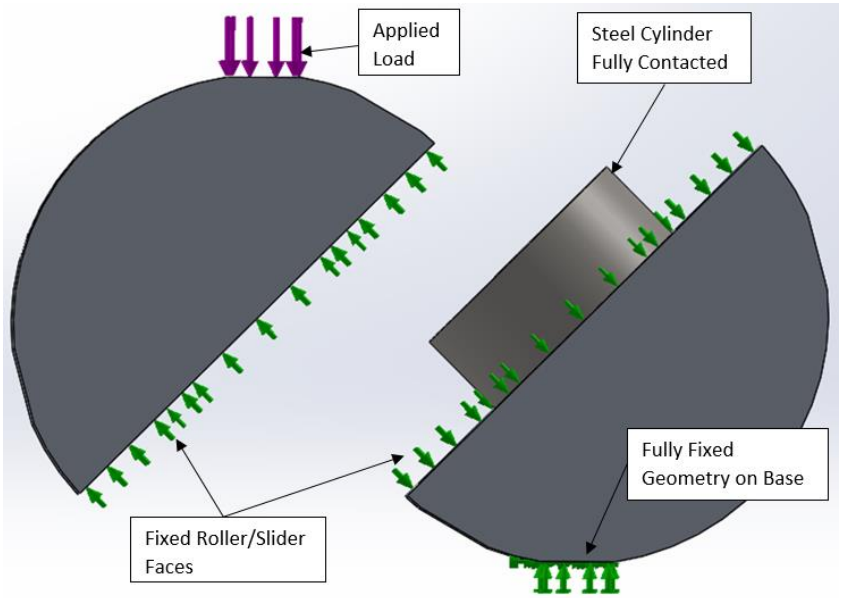


**Figure D. 7 - Loading simulation constraints on shear bond strength sample holder.**

Results from the simulation showed that when subjected to 1100lbf, (which is the maximum compressive strength of the Mark-10 load frame), a local stress concentration appears where the steel cylinders top edge makes contact to the inner wall of the top half, see Figure D.8. The von Mises value given to this area is around 1005psi, which is significantly lower than the yield strength value given for 6061 aluminum of 7998 psi (as noted in the Solidworks software material properties). In fact, the stress concentration at that point does not approach the yield strength until 8750lbf is applied to the system, see Figure D. 9.

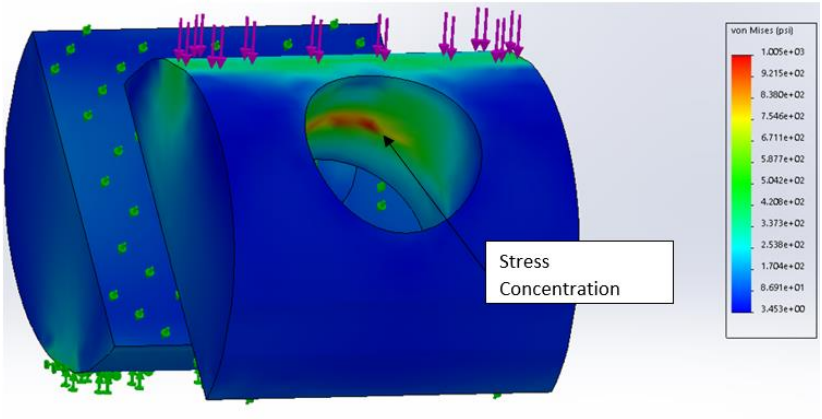


**Figure D. 8 – von Mises stress matrix simulation on shear bond test sample holder under load of 1100lbf.**

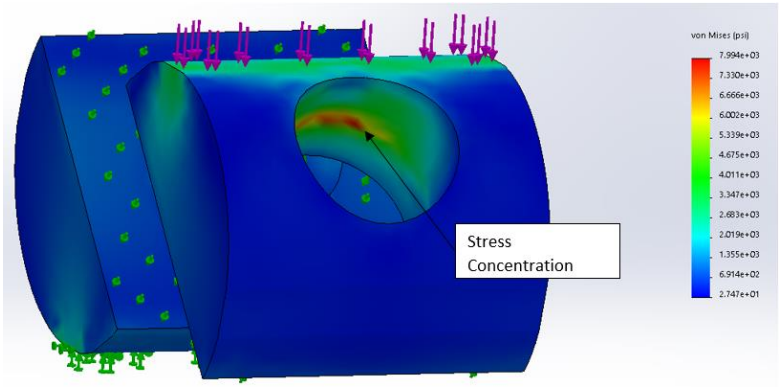


**Figure D. 9 - Von Mises stress simulation os shear bond test sample holder under 8750lbf of load.**

It was concluded from these simulations that the testing apparatus is fully capable of handling the full load range of the Mark-10 load frame, and if it is necessary, loads of up to 8750lbf can be applied without plastic deformation of the aluminum occurring. It should also be reiterated here that the limits stated were derived using an inclusion significantly harder than the cement. In other words, the formation of the stress concentrations seen in this model are unlikely because the cement would yield and distribute the load. Furthermore, the limit of 8750lbf is set to protect the sample holders in the event that the sample was incorrectly placed and the steel coin was preventing displacement.

## Appendix E

Appendix E provides an overview of the design iterations and final solution in testing the tensile bond strength samples.

The biggest challenge in creating a set up to evaluate the tensile bond strength at the cement/steel interface was connecting the load frame to the cement side such that it could apply the load normally to the interacting plane without creating points of high stress concentration in the cement. Initially, an anchor was set within the cement body (shown in Figure E. 1 and Figure E. 2) with the working premises being that the cement would bond with the steel anchor similar to the steel substrate; and as load was applied to the anchor, it would distribute it evenly to the cement body.

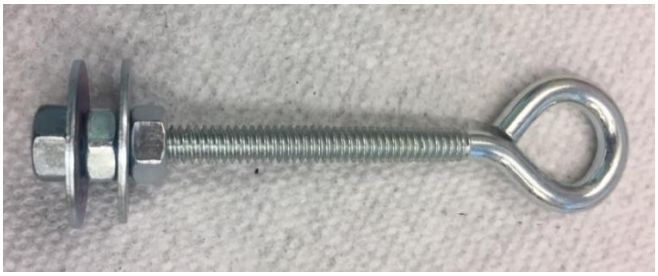

**Figure E. 1 - Tensile bond strength load frame connection anchor.**

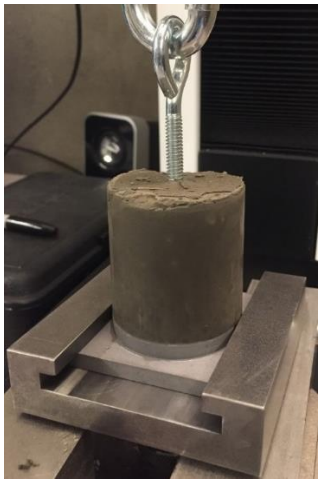

**Figure E. 2 - Tensile bond strength sample with anchor set within cement body before testing.**

What was found however, was that the load was only locally distributed to the cement in the immediate vicinity of the anchor which then created stress concentration points at the edge of these zones. The resulting failures then occurred beginning at the lowest point of the anchor and following the outer most edge of the anchor until the tensile strength of the cement body was over came. This type of failure is shown in Figure E. 3.

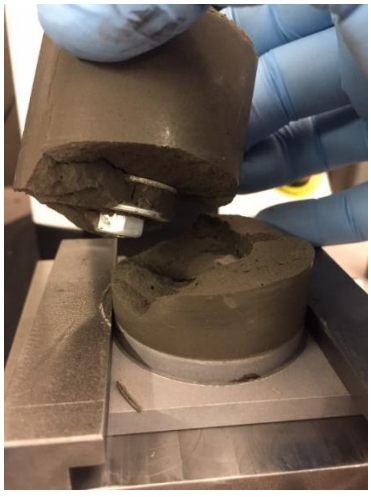

**Figure E. 3 - Tensile failure away from bonded plane.**

In an effort to distribute the load evenly across the cement body, a threaded connection point was then welded to the center of a steel coin and an epoxy was used to adhere it to the cement top. This testing consistently resulted in failure at the epoxied surface as opposed to the cement/steel interface. What was noted in this iteration however, was that was no failure within the cement body observed which was interpreted to mean that the load was being distributed evenly. Taking this into consideration, two changes to the design were then made.

The first change was purchasing a higher strength epoxy that was slightly less viscous in order to provide a better bond to the cement. The other change was reducing the size of the bonding plane between the cement and steel substrate. Reducing the area here allowed to artificially reduce the theoretical force that would be required to cause failure and as such reduce the likelihood that failure would occur anywhere else.

Changing the epoxy and bond area proved effective in testing the tensile bond strength. However, because of the now reduced bonding area, the samples became much more fragile and had a tendency to fail when being prepped as described in section 3.2.5. This lead to spots in the data that should be evaluated further before conclusive tensile bond strength values should be assigned to the respective cement recipes.

## Appendix F

Appendix F provides a tabular overview of the raw data discussed in this thesis.

**Table F. 1 - Base case UCS sample results.**

| Unconfined Compressive Strength Results (Cured for 28 Days at 194°F) | | | | | | | | | | | | |
|---|---|---|---|---|---|---|---|---|---|---|---|---|
| **Base Case** | Length (in) | | | | Length Deviation (in) | Diameter (in) | | | | L/D Ratio | Failure Load (lbf) | Compressive Strength (psi) |
| Sample # | 1 | 2 | 3 | Average | | 1 | 2 | 3 | Average | | | |
| 1 | 3.724 | 3.722 | 3.725 | 3.724 | 0.004 | 1.998 | 1.999 | 2.007 | 2.001 | 1.86 | 16454 | 5231 |
| 2 | 3.676 | 3.672 | 3.678 | 3.675 | 0.006 | 1.998 | 1.999 | 2.007 | 2.001 | 1.84 | 15692 | 4989 |
| 3 | 3.632 | 3.630 | 3.630 | 3.631 | 0.002 | 1.998 | 1.999 | 2.007 | 2.001 | 1.81 | 16663 | 5298 |
| 4 | 3.676 | 3.679 | 3.685 | 3.680 | 0.009 | 1.998 | 1.999 | 2.007 | 2.001 | 1.84 | 14589 | 4639 |

**Table F. 2 - Nanoparticle barite UCS sample results.**

| Unconfined Compressive Strength Results (Cured for 28 Days at 194°F) | | | | | | | | | | | | |
|---|---|---|---|---|---|---|---|---|---|---|---|---|
| **NP Barite** | Length (in) | | | | Length | Diameter (in) | | | | L/D Ratio | Failure | Compressive |
| Concentration (BWOC) | 1 | 2 | 3 | Average | Deviation (in) | 1 | 2 | 3 | Average | | Load (lbf) | Strength (psi) |
| 1% | 3.651 | 3.657 | 3.655 | 3.654 | 0.006 | 1.998 | 2.001 | 1.993 | 1.997 | 1.83 | 15472 | 4940 |
| 1% | 3.604 | 3.603 | 3.610 | 3.606 | 0.007 | 1.998 | 2.001 | 1.993 | 1.997 | 1.81 | 17060 | 5447 |
| 1% | 3.633 | 3.639 | 3.631 | 3.634 | 0.008 | 1.998 | 2.001 | 1.993 | 1.997 | 1.82 | 13578 | 4335 |
| 1% | 3.646 | 3.645 | 3.646 | 3.645 | 0.002 | 1.998 | 2.001 | 1.993 | 1.997 | 1.83 | 14714 | 4698 |
| 3% | 3.474 | 3.473 | 3.472 | 3.473 | 0.002 | 1.985 | 1.986 | 1.989 | 1.987 | 1.75 | 12282 | 3963 |
| 3% | 3.676 | 3.682 | 3.675 | 3.677 | 0.007 | 1.985 | 1.986 | 1.989 | 1.987 | 1.85 | 18250 | 5888 |
| 3% | 3.608 | 3.611 | 3.611 | 3.610 | 0.004 | 1.985 | 1.986 | 1.989 | 1.987 | 1.82 | 17759 | 5730 |
| 3% | 3.561 | 3.552 | 3.556 | 3.556 | 0.010 | 1.985 | 1.986 | 1.989 | 1.987 | 1.79 | 11997 | 3871 |
| 5% | 3.571 | 3.554 | 3.557 | 3.560 | 0.017 | 1.983 | 2.008 | 2.001 | 1.997 | 1.78 | 15589 | 4976 |
| 5% | 3.617 | 3.623 | 3.617 | 3.619 | 0.007 | 1.983 | 2.008 | 2.001 | 1.997 | 1.81 | 17259 | 5509 |
| 5% | 3.629 | 3.639 | 3.636 | 3.634 | 0.011 | 1.983 | 2.008 | 2.001 | 1.997 | 1.82 | 18151 | 5794 |
| 5% | 3.685 | 3.682 | 3.683 | 3.683 | 0.003 | 1.983 | 2.008 | 2.001 | 1.997 | 1.84 | 17160 | 5478 |

**Table F. 3 - Nanoparticle magnetite UCS sample results.**

| Unconfined Compressive Strength Results (Cured for 28 Days at 194°F) | | | | | | | | | | | | |
|---|---|---|---|---|---|---|---|---|---|---|---|---|
| **NP Magnetite** | Length (in) | | | | Length | Diameter (in) | | | | L/D Ratio | Failure | Compressive |
| Concentration (BWOC) | 1 | 2 | 3 | Average | Deviation (in) | 1 | 2 | 3 | Average | | Load (lbf) | Strength (psi) |
| 1% | 3.615 | 3.617 | 3.619 | 3.617 | 0.004 | 1.993 | 1.988 | 1.991 | 1.991 | 1.82 | 19455 | 6252 |
| 1% | 3.741 | 3.735 | 3.735 | 3.737 | 0.006 | 1.993 | 1.988 | 1.991 | 1.991 | 1.88 | 17395 | 5590 |
| 1% | 3.726 | 3.720 | 3.722 | 3.723 | 0.005 | 1.993 | 1.988 | 1.991 | 1.991 | 1.87 | 20826 | 6693 |
| 1% | 3.619 | 3.613 | 3.613 | 3.615 | 0.006 | 1.993 | 1.988 | 1.991 | 1.991 | 1.82 | 19342 | 6216 |
| 3% | 3.675 | 3.669 | 3.681 | 3.675 | 0.012 | 1.990 | 1.996 | 2.002 | 1.996 | 1.84 | 15909 | 5086 |
| 3% | 3.589 | 3.590 | 3.591 | 3.590 | 0.002 | 1.990 | 1.996 | 2.002 | 1.996 | 1.80 | 17815 | 5695 |
| 3% | 3.654 | 3.661 | 3.661 | 3.659 | 0.007 | 1.990 | 1.996 | 2.002 | 1.996 | 1.83 | 17940 | 5735 |
| 3% | 3.646 | 3.649 | 3.652 | 3.649 | 0.006 | 1.990 | 1.996 | 2.002 | 1.996 | 1.83 | 17242 | 5512 |
| 5% | 3.661 | 3.656 | 3.659 | 3.659 | 0.006 | 1.998 | 1.990 | 1.999 | 1.996 | 1.83 | 18316 | 5855 |
| 5% | 3.701 | 3.706 | 3.709 | 3.705 | 0.008 | 1.998 | 1.990 | 1.999 | 1.996 | 1.86 | 20182 | 6452 |
| 5% | 3.678 | 3.686 | 3.676 | 3.680 | 0.010 | 1.998 | 1.990 | 1.999 | 1.996 | 1.84 | 19134 | 6117 |
| 5% | 3.674 | 3.680 | 3.684 | 3.679 | 0.010 | 1.998 | 1.990 | 1.999 | 1.996 | 1.84 | 18823 | 6018 |

**Table F. 4 - Base case Brazilian test sample results.**

| Brazilian Test for Tensile Strength Results (Cured for 28 Days at 194°F) | | | | | | | | | | | | | |
|---|---|---|---|---|---|---|---|---|---|---|---|---|---|
| **Base Case** | Thickness (in) | | | | Thickness Deviation (in) | Diameter (in) | | | | Mass (lb) | Density (lb/ft^3) | Failure Load (lbf) | Tensile Strength (psi) |
| Sample # | 1 | 2 | 3 | Average | | 1 | 2 | 3 | Average | | | | |
| 1 | 1.007 | 1.006 | 1.007 | 1.006 | 0.001 | 1.990 | 1.990 | 1.988 | 1.989 | 0.2365 | 130.7 | 3628 | 1154 |
| 2 | 1.007 | 1.002 | 1.002 | 1.004 | 0.005 | 1.995 | 2.002 | 1.998 | 1.998 | 0.2348 | 129.0 | 3211 | 1020 |
| 3 | 0.997 | 1.008 | 0.992 | 0.999 | 0.016 | 1.992 | 1.996 | 1.987 | 1.992 | 0.2340 | 130.0 | 2628 | 841 |
| 4 | 0.998 | 1.009 | 1.005 | 1.004 | 0.011 | 1.971 | 1.969 | 1.971 | 1.970 | 0.2384 | 134.7 | 4144 | 1334 |
| 5 | 1.011 | 1.019 | 1.001 | 1.010 | 0.018 | 1.994 | 1.993 | 1.988 | 1.992 | 0.2366 | 129.9 | 3325 | 1052 |
| 6 | 1.005 | 0.996 | 0.999 | 1.000 | 0.009 | 1.997 | 1.995 | 2.000 | 1.997 | 0.2340 | 129.1 | 2475 | 789 |

**Table F. 5 - Nanoparticle barite Brazilian test sample results.**

| Brazilian Test for Tensile Strength Results (Cured for 28 Days at 194°F) | | | | | | | | | | | | | |
|---|---|---|---|---|---|---|---|---|---|---|---|---|---|
| **NP Barite** | Thickness (in) | | | | Thickness Deviation (in) | Diameter (in) | | | | Mass (lb) | Density (lb/ft^3) | Failure Load (lbf) | Tensile Strength (psi) |
| Concentration (BWOC) | 1 | 2 | 3 | Average | | 1 | 2 | 3 | Average | | | | |
| 1% | 0.999 | 1.001 | 1.001 | 1.000 | 0.002 | 1.997 | 1.998 | 1.996 | 1.997 | 0.2326 | 128.3 | 2784 | 887 |
| 1% | 0.997 | 0.998 | 1.004 | 0.999 | 0.007 | 1.989 | 1.996 | 1.993 | 1.992 | 0.2331 | 129.3 | 3000 | 959 |
| 1% | 1.002 | 1.009 | 0.997 | 1.002 | 0.012 | 1.989 | 1.986 | 1.987 | 1.987 | 0.2365 | 131.5 | 3764 | 1203 |
| 1% | 1.011 | 1.008 | 1.006 | 1.008 | 0.005 | 1.991 | 1.993 | 1.991 | 1.992 | 0.2337 | 128.6 | 2328 | 738 |
| 1% | 0.999 | 1.007 | 1.006 | 1.004 | 0.008 | 2.000 | 1.994 | 1.997 | 1.997 | 0.2327 | 127.9 | 2291 | 727 |
| 1% | 1.007 | 1.002 | 1.003 | 1.004 | 0.004 | 1.989 | 1.987 | 1.987 | 1.987 | 0.2349 | 130.4 | 3287 | 1049 |
| 3% | 1.003 | 0.997 | 1.001 | 1.000 | 0.006 | 1.989 | 1.999 | 1.998 | 1.995 | 0.2278 | 125.9 | 2467 | 787 |
| 3% | 1.002 | 1.003 | 1.002 | 1.002 | 0.000 | 2.000 | 1.987 | 1.986 | 1.991 | 0.2314 | 128.2 | 2344 | 748 |
| 3% | 1.006 | 1.004 | 1.003 | 1.004 | 0.003 | 1.991 | 1.988 | 1.995 | 1.991 | 0.2303 | 127.3 | 2243 | 714 |
| 3% | 0.995 | 0.996 | 0.997 | 0.996 | 0.002 | 1.985 | 1.990 | 1.987 | 1.987 | 0.2316 | 129.6 | 2438 | 784 |
| 3% | 1.004 | 1.001 | 0.995 | 1.000 | 0.009 | 1.990 | 1.986 | 1.985 | 1.987 | 0.2325 | 129.6 | 2579 | 827 |
| 3% | 1.001 | 0.997 | 1.000 | 0.999 | 0.004 | 1.995 | 1.989 | 2.005 | 1.996 | 0.2314 | 127.9 | 2457 | 784 |
| 5% | 1.002 | 1.012 | 1.003 | 1.006 | 0.010 | 2.006 | 1.988 | 2.003 | 1.999 | 0.2327 | 127.4 | 2650 | 839 |
| 5% | 1.007 | 1.001 | 1.003 | 1.003 | 0.006 | 1.992 | 2.001 | 1.989 | 1.994 | 0.2335 | 128.8 | 3027 | 963 |
| 5% | 0.998 | 1.000 | 1.007 | 1.001 | 0.009 | 1.983 | 1.983 | 1.986 | 1.984 | 0.2360 | 131.8 | 3061 | 981 |
| 5% | 1.008 | 1.008 | 1.009 | 1.008 | 0.001 | 1.995 | 1.992 | 2.005 | 1.997 | 0.2338 | 127.9 | 2350 | 743 |
| 5% | 0.994 | 0.997 | 1.003 | 0.998 | 0.009 | 1.986 | 1.997 | 1.996 | 1.993 | 0.2317 | 128.6 | 2821 | 903 |
| 5% | 0.997 | 1.003 | 1.008 | 1.003 | 0.011 | 1.986 | 1.989 | 1.990 | 1.988 | 0.2356 | 130.8 | 3015 | 963 |

**Table F. 6 - Nanoparticle magnetite Brazilian test sample results.**

| Brazilian Test for Tensile Strength Results (Cured for 28 Days at 194°F) | | | | | | | | | | | | | |
|---|---|---|---|---|---|---|---|---|---|---|---|---|---|
| **NP Magnetite** | Thickness (in) | | | | Thickness Deviation (in) | Diameter (in) | | | | Mass (lb) | Density (lb/ft^3) | Failure Load (lbf) | Tensile Strength (psi) |
| Concentration (BWOC) | 1 | 2 | 3 | Average | | 1 | 2 | 3 | Average | | | | |
| 1% | 1.012 | 1.004 | 1.006 | 1.007 | 0.008 | 1.988 | 1.996 | 1.993 | 1.992 | 0.2322 | 127.8 | 3054 | 969 |
| 1% | 1.002 | 1.012 | 1.006 | 1.007 | 0.010 | 1.993 | 2.001 | 2.005 | 1.999 | 0.2337 | 127.8 | 2224 | 704 |
| 1% | 1.003 | 1.004 | 1.002 | 1.003 | 0.002 | 1.991 | 1.991 | 1.990 | 1.990 | 0.2324 | 128.7 | 2981 | 951 |
| 1% | 1.002 | 1.007 | 1.001 | 1.003 | 0.006 | 1.986 | 1.983 | 1.983 | 1.984 | 0.2346 | 130.8 | 2879 | 921 |
| 1% | 0.999 | 1.002 | 1.002 | 1.001 | 0.003 | 1.990 | 1.996 | 2.003 | 1.996 | 0.2325 | 128.3 | 2525 | 805 |
| 1% | 1.000 | 0.998 | 1.005 | 1.001 | 0.007 | 1.982 | 1.983 | 1.985 | 1.983 | 0.2337 | 130.7 | 2682 | 860 |
| 3% | 0.980 | 0.983 | 0.980 | 0.981 | 0.003 | 1.997 | 1.997 | 1.999 | 1.997 | 0.2282 | 128.3 | 2388 | 776 |
| 3% | 1.004 | 1.015 | 1.000 | 1.006 | 0.015 | 1.984 | 1.988 | 1.985 | 1.985 | 0.2342 | 129.9 | 2810 | 895 |
| 3% | 0.993 | 0.988 | 0.990 | 0.990 | 0.005 | 1.992 | 1.988 | 1.988 | 1.989 | 0.2298 | 129.1 | 2375 | 768 |
| 3% | 1.003 | 1.008 | 1.004 | 1.005 | 0.005 | 1.997 | 1.997 | 1.991 | 1.995 | 0.2332 | 128.4 | 2555 | 812 |
| 3% | 1.005 | 1.003 | 0.998 | 1.002 | 0.006 | 1.988 | 1.989 | 1.985 | 1.987 | 0.2346 | 130.5 | 3097 | 991 |
| 3% | 1.003 | 0.998 | 1.001 | 1.000 | 0.005 | 1.989 | 1.991 | 1.993 | 1.991 | 0.2323 | 128.9 | 2716 | 868 |
| 5% | 1.003 | 1.007 | 1.010 | 1.007 | 0.008 | 1.986 | 1.987 | 1.989 | 1.987 | 0.2370 | 131.2 | 2003 | 638 |
| 5% | 0.989 | 0.997 | 0.997 | 0.994 | 0.008 | 1.998 | 1.994 | 1.993 | 1.995 | 0.2317 | 128.9 | 2830 | 908 |
| 5% | 1.001 | 1.000 | 1.004 | 1.002 | 0.004 | 1.988 | 1.992 | 1.988 | 1.989 | 0.2331 | 129.4 | 2526 | 807 |
| 5% | 1.017 | 1.007 | 1.007 | 1.010 | 0.010 | 1.988 | 1.997 | 2.001 | 1.995 | 0.2342 | 128.2 | 2406 | 760 |
| 5% | 1.004 | 1.000 | 1.010 | 1.004 | 0.010 | 1.975 | 1.984 | 1.984 | 1.981 | 0.2363 | 131.9 | 3191 | 1021 |
| 5% | 1.008 | 1.009 | 1.005 | 1.007 | 0.004 | 1.993 | 1.992 | 1.991 | 1.992 | 0.2338 | 128.8 | 2980 | 946 |

**Table F. 7 - Base case shear bond strength sample results.**

| Shear Bond Strength ~Base Case | | | | | | | |
|---|---|---|---|---|---|---|---|
| Sample # | Area 'A' (in^2) | Load @ Failure (lbf) | Normal Load F_N (lbf) | Fric. Const. | Fric. Force (lbf) | Shear Load 'F_τ' (lbf) | Shear Strength 'σ_τ' (psi) |
| 1 | 3.14 | 229.0 | 59.3 | 0.3 | 17.8 | 221.2 | 64.7 |
| 2 | 3.14 | 228.5 | 59.1 | 0.3 | 17.7 | 220.7 | 64.6 |
| 3 | 3.14 | 204.0 | 52.8 | 0.3 | 15.8 | 197.0 | 57.7 |
| 4 | 3.14 | 176.0 | 45.6 | 0.3 | 13.7 | 170.0 | 49.8 |
| 5 | 3.14 | 222.5 | 57.6 | 0.3 | 17.3 | 214.9 | 62.9 |
| 6 | 3.14 | 258.0 | 66.8 | 0.3 | 20.0 | 249.2 | 72.9 |
| 7 | 3.14 | 186.0 | 48.1 | 0.3 | 14.4 | 179.7 | 52.6 |
| 8 | 3.14 | 300.5 | 77.8 | 0.3 | 23.3 | 290.3 | 85.0 |

**Table F. 8 - Nanoparticle barite shear bond strength sample results.**

| Shear Bond Strength ~NP Barite | | | | | | | |
|---|---|---|---|---|---|---|---|
| Concentration (BWOC) | Area 'A' (in^2) | Load @ Failure (lbf) | Normal Load F_N (lbf) | Fric. Const. | Fric. Force (lbf) | Shear Load 'F_τ' (lbf) | Shear Strength 'σ_τ' (psi) |
| 1% | 3.14 | 210.5 | 54.5 | 0.3 | 16.3 | 203.3 | 59.5 |
| 1% | 3.14 | 225.5 | 58.4 | 0.3 | 17.5 | 217.8 | 63.8 |
| 1% | 3.14 | 221.0 | 57.2 | 0.3 | 17.2 | 213.5 | 62.5 |
| 1% | 3.14 | 244.5 | 63.3 | 0.3 | 19.0 | 236.2 | 69.1 |
| 1% | 3.14 | 252.0 | 65.2 | 0.3 | 19.6 | 243.4 | 71.3 |
| 1% | 3.14 | 278.5 | 72.1 | 0.3 | 21.6 | 269.0 | 78.7 |
| 1% | 3.14 | 239.0 | 61.9 | 0.3 | 18.6 | 230.9 | 67.6 |
| 1% | 3.14 | 235.5 | 61.0 | 0.3 | 18.3 | 227.5 | 66.6 |
| 3% | 3.14 | 294.5 | 76.2 | 0.3 | 22.9 | 284.5 | 83.3 |
| 3% | 3.14 | 187.5 | 48.5 | 0.3 | 14.6 | 181.1 | 53.0 |
| 3% | 3.14 | 236.0 | 61.1 | 0.3 | 18.3 | 228.0 | 66.7 |
| 3% | 3.14 | 253.5 | 65.6 | 0.3 | 19.7 | 244.9 | 71.7 |
| 3% | 3.14 | 174.5 | 45.2 | 0.3 | 13.5 | 168.6 | 49.3 |
| 3% | 3.14 | 261.5 | 67.7 | 0.3 | 20.3 | 252.6 | 73.9 |
| 3% | 3.14 | 416.0 | 107.7 | 0.3 | 32.3 | 401.8 | 117.6 |
| 3% | 3.14 | 346.0 | 89.6 | 0.3 | 26.9 | 334.2 | 97.8 |
| 5% | 3.14 | 258.5 | 66.9 | 0.3 | 20.1 | 249.7 | 73.1 |
| 5% | 3.14 | 253.5 | 65.6 | 0.3 | 19.7 | 244.9 | 71.7 |
| 5% | 3.14 | 245.0 | 63.4 | 0.3 | 19.0 | 236.7 | 69.3 |
| 5% | 3.14 | 229.5 | 59.4 | 0.3 | 17.8 | 221.7 | 64.9 |
| 5% | 3.14 | 250.5 | 64.8 | 0.3 | 19.5 | 242.0 | 70.8 |
| 5% | 3.14 | 507.0 | 131.2 | 0.3 | 39.4 | 489.7 | 143.4 |
| 5% | 3.14 | 371.5 | 96.2 | 0.3 | 28.8 | 358.8 | 105.0 |
| 5% | 3.14 | 548.0 | 141.8 | 0.3 | 42.5 | 529.3 | 154.9 |

**Table F. 9 - Nanoparticle magnetite shear bond strength sample results.**

| Shear Bond Strength ~NP Magnetite | | | | | | | |
|---|---|---|---|---|---|---|---|
| Concentration (BWOC) | Area 'A' (in^2) | Load @ Failure (lbf) | Normal Load F_N (lbf) | Fric. Const. | Fric. Force (lbf) | Shear Load 'F_τ' (lbf) | Shear Strength 'σ_τ' (psi) |
| 1% | 3.14 | 272.5 | 70.5 | 0.3 | 21.2 | 263.2 | 77.0 |
| 1% | 3.14 | 195.5 | 50.6 | 0.3 | 15.2 | 188.8 | 55.3 |
| 1% | 3.14 | 231.5 | 59.9 | 0.3 | 18.0 | 223.6 | 65.5 |
| 1% | 3.14 | 264.5 | 68.5 | 0.3 | 20.5 | 255.5 | 74.8 |
| 1% | 3.14 | 232.0 | 60.0 | 0.3 | 18.0 | 224.1 | 65.6 |
| 1% | 3.14 | 238.0 | 61.6 | 0.3 | 18.5 | 229.9 | 67.3 |
| 1% | 3.14 | 262.0 | 67.8 | 0.3 | 20.3 | 253.1 | 74.1 |
| 1% | 3.14 | 242.0 | 62.6 | 0.3 | 18.8 | 233.8 | 68.4 |
| 3% | 3.14 | 253.5 | 65.6 | 0.3 | 19.7 | 244.9 | 71.7 |
| 3% | 3.14 | 253.0 | 65.5 | 0.3 | 19.6 | 244.4 | 71.5 |
| 3% | 3.14 | 243.5 | 63.0 | 0.3 | 18.9 | 235.2 | 68.8 |
| 3% | 3.14 | 226.0 | 58.5 | 0.3 | 17.5 | 218.3 | 63.9 |
| 3% | 3.14 | 233.5 | 60.4 | 0.3 | 18.1 | 225.5 | 66.0 |
| 3% | 3.14 | 327.5 | 84.8 | 0.3 | 25.4 | 316.3 | 92.6 |
| 3% | 3.14 | 360.0 | 93.2 | 0.3 | 28.0 | 347.7 | 101.8 |
| 3% | 3.14 | 375.0 | 97.1 | 0.3 | 29.1 | 362.2 | 106.0 |
| 5% | 3.14 | 356.0 | 92.1 | 0.3 | 27.6 | 343.9 | 100.7 |
| 5% | 3.14 | 365.0 | 94.5 | 0.3 | 28.3 | 352.6 | 103.2 |
| 5% | 3.14 | 359.5 | 93.0 | 0.3 | 27.9 | 347.3 | 101.6 |
| 5% | 3.14 | 342.0 | 88.5 | 0.3 | 26.6 | 330.3 | 96.7 |
| 5% | 3.14 | 287.0 | 74.3 | 0.3 | 22.3 | 277.2 | 81.1 |
| 5% | 3.14 | 296.5 | 76.7 | 0.3 | 23.0 | 286.4 | 83.8 |
| 5% | 3.14 | 513.5 | 132.9 | 0.3 | 39.9 | 496.0 | 145.2 |
| 5% | 3.14 | 387.5 | 100.3 | 0.3 | 30.1 | 374.3 | 109.6 |

**Table F. 10 - Tensile bond strength and load at failure results.**

| Tensile Bond Strength | | | | | | |
|---|---|---|---|---|---|---|
| Cement Sample | Tensile Load (lbf) | Diameter 1 (in) | Diameter 2 (in) | Diameter 3 (in) | Observed Tensile Bond Strength (psi) | Change from Base Case (%) |
| Base Case | 87 | 0.979 | 0.9755 | 0.9975 | 114.403464 | 0% |
| 1% NP Barite 1 | 103 | - | - | - | Tensile Failure | - |
| 3% NP Barite 1 | 126 | - | - | - | Tensile Failure | - |
| 3% NP Barite | 107.5 | 0.9755 | 1 | 0.988 | 140.2656179 | 20% |
| 5% NP Barite 1 | 163.5 | - | - | - | Tensile Failure | - |
| 5% NP Barite 2 | 122.5 | - | - | - | Tensile Failure | - |
| 1% NP Magnetite 1 | 124.5 | 0.98175 | 0.987875 | 0.989 | 162.9829349 | 35% |
| 1% NP Magnetite 2 | 100 | 0.9745 | 0.9865 | 0.991 | 131.4982344 | 14% |
| 3% NP Magnetite | 108.5 | 0.998 | 0.9895 | 0.9795 | 141.2366063 | 21% |
| 5% NP Magnetite 1 | 101 | - | - | - | Tensile Failure | - |
| 5% NP Magnetite 2 | 195.5 | - | - | - | Tensile Failure | - |

**Table F. 11 - Young's Modulus calculations.**

| | Youngs Modulus (E) Results | | | | | | | | | |
|---|---|---|---|---|---|---|---|---|---|---|
| | Sample # | Failure Load (lbf) | 35% Failure Load (lbf) | e1 (%) | S1 (psi) | 45% Failure Load (lbf) | e2 (%) | S2 (psi) | E (ksi) | UCS (psi) |
| Base Case | 1 | 16454 | 5761 | 0.391 | 1834 | 7409 | 0.454 | 2358 | 829 | 5231 |
| Base Case | 2 | 15692 | 5492 | 0.371 | 1748 | 7059 | 0.428 | 2247 | 869 | 4989 |
| Base Case | 3 | 16663 | 5831 | 0.357 | 1856 | 7497 | 0.419 | 2386 | 855 | 5298 |
| Base Case | 4 | 14589 | 5106 | 0.343 | 1625 | 6569 | 0.397 | 2091 | 858 | 4639 |
| 1% NP Barite | 1 | 15472 | 5416 | 0.344 | 1724 | 6964 | 0.399 | 2217 | 891 | 4940 |
| 1% NP Barite | 2 | 17060 | 5968 | 0.379 | 1900 | 7679 | 0.442 | 2444 | 872 | 5447 |
| 1% NP Barite | 3 | 13578 | 4752 | 0.312 | 1513 | 6112 | 0.364 | 1946 | 844 | 4335 |
| 1% NP Barite | 4 | 14720 | 5153 | 0.360 | 1640 | 6626 | 0.416 | 2109 | 843 | 4698 |
| 3% NP Barite | 1 | 12282 | 4302 | 0.321 | 1369 | 5529 | 0.377 | 1760 | 692 | 3963 |
| 3% NP Barite | 2 | 18250 | 6388 | 0.387 | 2033 | 8209 | 0.450 | 2613 | 920 | 5888 |
| 3% NP Barite | 3 | 17759 | 6213 | 0.315 | 1978 | 7994 | 0.377 | 2544 | 912 | 5730 |
| 3% NP Barite | 4 | 11997 | 4197 | 0.289 | 1336 | 5398 | 0.341 | 1718 | 730 | 3871 |
| 5% NP Barite | 1 | 15589 | 4456 | 0.303 | 1418 | 7012 | 0.395 | 2232 | 885 | 4976 |
| 5% NP Barite | 2 | 17259 | 6042 | 0.374 | 1923 | 7769 | 0.435 | 2473 | 901 | 5509 |
| 5% NP Barite | 3 | 18151 | 6352 | 0.349 | 2022 | 8171 | 0.412 | 2601 | 915 | 5794 |
| 5% NP Barite | 4 | 17160 | 6006 | 0.383 | 1912 | 7725 | 0.446 | 2459 | 871 | 5478 |
| 1% NP Magnetite | 1 | 19455 | 6808 | 0.415 | 2167 | 8756 | 0.481 | 2787 | 938 | 6252 |
| 1% NP Magnetite | 2 | 17395 | 6089 | 0.469 | 1938 | 7828 | 0.535 | 2492 | 843 | 5590 |
| 1% NP Magnetite | 3 | 20826 | 7286 | 0.456 | 2319 | 9371 | 0.529 | 2983 | 915 | 6693 |
| 1% NP Magnetite | 4 | 19342 | 6770 | 0.443 | 2155 | 8703 | 0.511 | 2770 | 901 | 6216 |
| 3%NP Magnetite | 1 | 15909 | 5569 | 0.388 | 1773 | 7160 | 0.452 | 2279 | 789 | 5086 |
| 3%NP Magnetite | 2 | 17815 | 6236 | 0.427 | 1985 | 8019 | 0.508 | 2553 | 701 | 5695 |
| 3%NP Magnetite | 3 | 17940 | 6280 | 0.359 | 1999 | 8068 | 0.419 | 2568 | 944 | 5735 |
| 3%NP Magnetite | 4 | 17241 | 6035 | 0.408 | 1921 | 7758 | 0.475 | 2469 | 821 | 5512 |
| 5% NP Magnetite | 1 | 18316 | 6411 | 0.413 | 2041 | 8245 | 0.478 | 2624 | 894 | 5855 |
| 5% NP Magnetite | 2 | 20182 | 7063 | 0.356 | 2248 | 9084 | 0.420 | 2892 | 1012 | 6452 |
| 5% NP Magnetite | 3 | 19134 | 6698 | 0.373 | 2132 | 8610 | 0.439 | 2741 | 925 | 6117 |
| 5% NP Magnetite | 4 | 18823 | 6589 | 0.367 | 2097 | 8469 | 0.431 | 2696 | 934 | 6018 |

## Appendix G

Appendix G describes the procedure used to acquire the Young's Modulus, as well as the values obtained for each sample.

To find the Young's Modulus of the cement, ASTM C469 was initially referenced and found not to be effective in this application due to the precision of the strain measurements of the load frame used. In an effort to adhere as closely as possible to the standard, the stress and strain points used to calculate the stiffness were taken at points ±5% of 40% of the ultimate load of the tested sample. This yielded slopes that best described the stiffness of each sample. The stiffness was then acquired using the following equation:

$$E = \frac{(S_2 - S_{1)}}{(e_2 - e_1)}$$

**Equation G. 1 - Young's Modulus calculation with selected points.**

Where:

| Variable | Description |
|---|---|
| $S_2, S_1$ | Are the stresses corresponding to 45% and 35% of the ultimate load respectively. |
| $e_2, e_1$ | Are the strains corresponding to 45% and 35% of the ultimate load respectively. |

The average results from these calculations for each cement recipe is given in Table G. 1 and the raw data and calculations are provided in appendix E.

**Table G. 1 - Averaged Young's Modulus results.**

| | Overall Young's Modulus Results | | |
|---|---|---|---|
| | Mean Young's Modulus (ksi) | CV (%) | Change from Base Case (%) |
| Base Case | 852.6 | 2.0% | - |
| 1% NP Barite | 862.4 | 2.7% | 1.1% |
| 3% NP Barite | 813.5 | 14.7% | -4.7% |
| 5% NP Barite | 892.9 | 2.1% | 4.6% |
| 1% NP Magnetite | 899.1 | 4.5% | 5.3% |
| 3%NP Magnetite | 813.6 | 12.4% | -4.7% |
| 5% NP Magnetite | 941.0 | 5.3% | 9.9% |

## Appendix H

Appendix H details the energy-dispersive spectroscopy results of tested Brazilian samples that have been cut to size and polished down to a 3µm finish using a diamond suspension. The bulk composition of several points for each sample has been evaluated at an SEM magnification of 1000x.

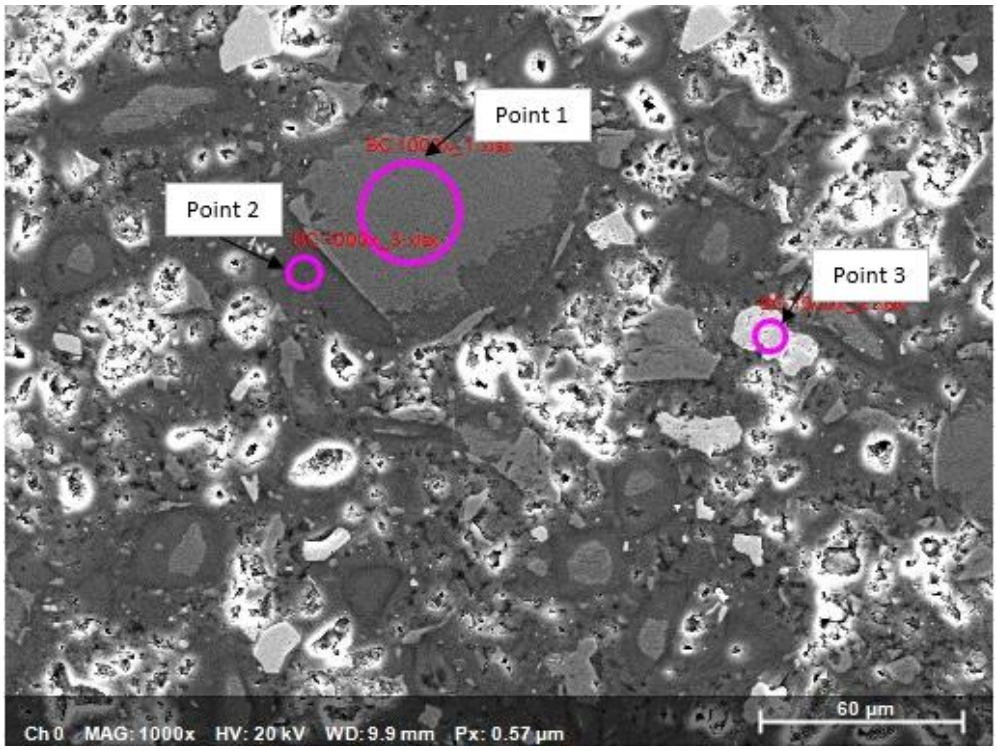


**Figure H. 1 - Points used in EDS evaluation for base case sample.**

**Table H. 1 – EDS results for base case sample.**

| | Base Case Bulk Composition (%) | | | | | | | |
|---|---|---|---|---|---|---|---|---|
| | Oxygen | Sodium | Aluminum | Silicon | Sulfur | Calcium | Iron | Barium |
| Point 1 | 50.64 | 0.02 | 0.87 | 11.73 | 0.23 | 35.54 | 0.50 | 0.48 |
| Point 2 | 63.98 | 0.07 | 0.87 | 8.69 | 0.47 | 24.91 | 0.91 | 0.10 |
| Point 3 | 63.03 | 0.00 | 0.25 | 2.18 | 13.84 | 7.62 | 0.21 | 12.87 |

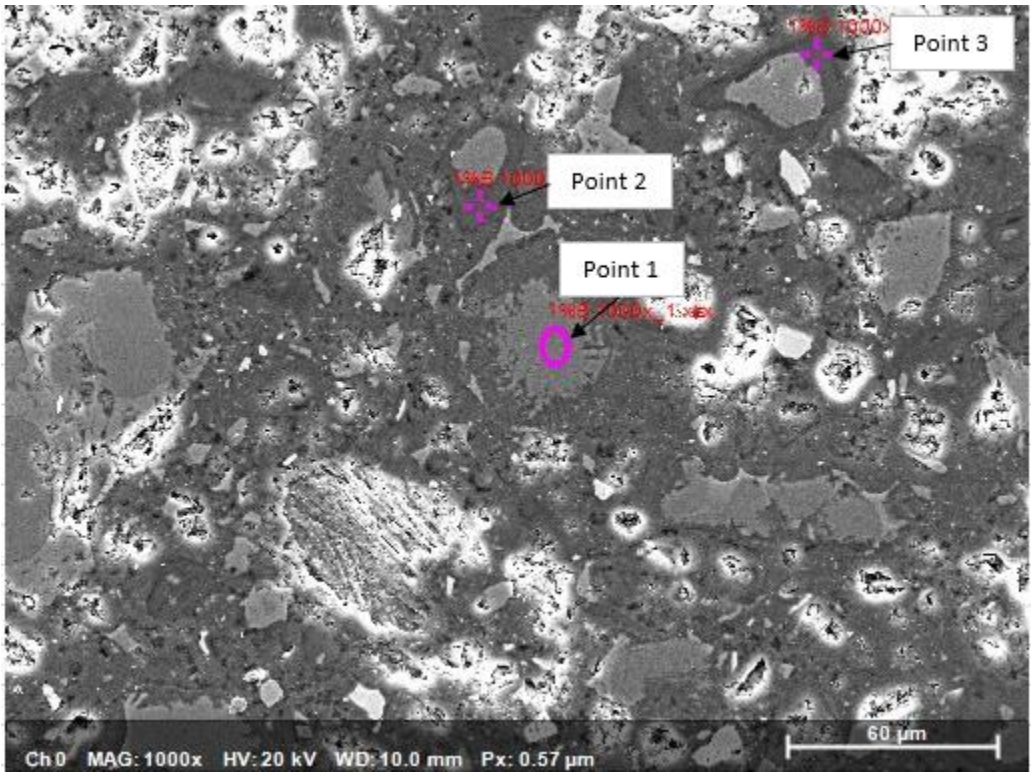


**Figure H. 2 - Points used for EDS evaluation of 1% BWOC nanoparticle barite sample.**

**Table H. 2 - EDS results for 1% BWOC nanoparticle barite sample.**

| | 1% BWOC Nanoparticle Barite Bulk Composition (%) | | | | | | | |
|---|---|---|---|---|---|---|---|---|
| | Oxygen | Sodium | Aluminum | Silicon | Sulfur | Calcium | Iron | Barium |
| Point 1 | 49.76 | 0.00 | 0.76 | 12.41 | 0.00 | 36.65 | 0.42 | 0.00 |
| Point 2 | 64.00 | 0.00 | 0.65 | 10.86 | 0.59 | 23.63 | 0.28 | 0.00 |
| Point 3 | 61.71 | 1.29 | 0.54 | 11.76 | 0.78 | 23.84 | 0.06 | 0.01 |

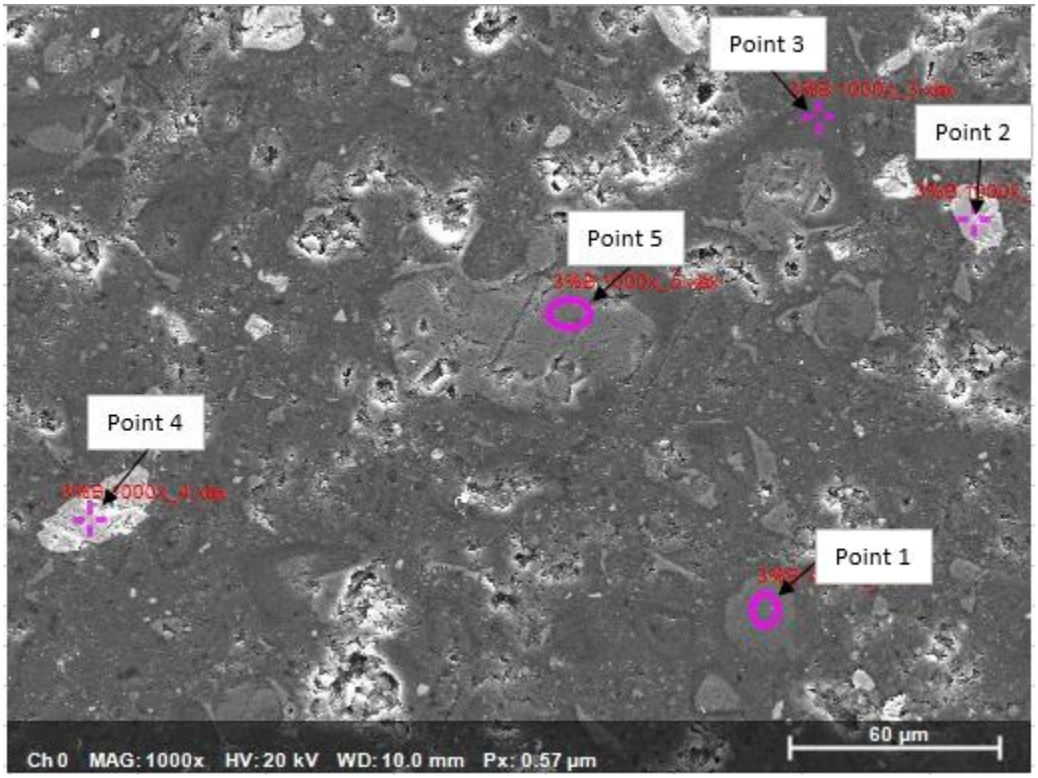


**Figure H. 3 - Points used in EDS evaluation of 3% BWOC nanoparticle barite sample.**

**Table H. 3 - EDS results for 3% BWOC nanoparticle barite sample.**

| | 3% BWOC Nanoparticle Barite Bulk Composition (%) | | | | | | | |
|---|---|---|---|---|---|---|---|---|
| | Oxygen | Sodium | Aluminum | Silicon | Sulfur | Calcium | Iron | Barium |
| Point 1 | 49.13 | 0.00 | 1.19 | 13.08 | 0.73 | 34.29 | 1.20 | 0.38 |
| Point 2 | 63.54 | 0.00 | 0.00 | 0.00 | 18.99 | 1.03 | 0.00 | 16.44 |
| Point 3 | 56.83 | 0.21 | 0.35 | 11.01 | 0.51 | 30.71 | 0.38 | 0.00 |
| Point 4 | 45.99 | 0.00 | 0.01 | 0.53 | 27.40 | 1.51 | 0.11 | 24.45 |
| Point 5 | 44.84 | 0.00 | 0.00 | 9.77 | 0.00 | 45.12 | 0.27 | 0.00 |

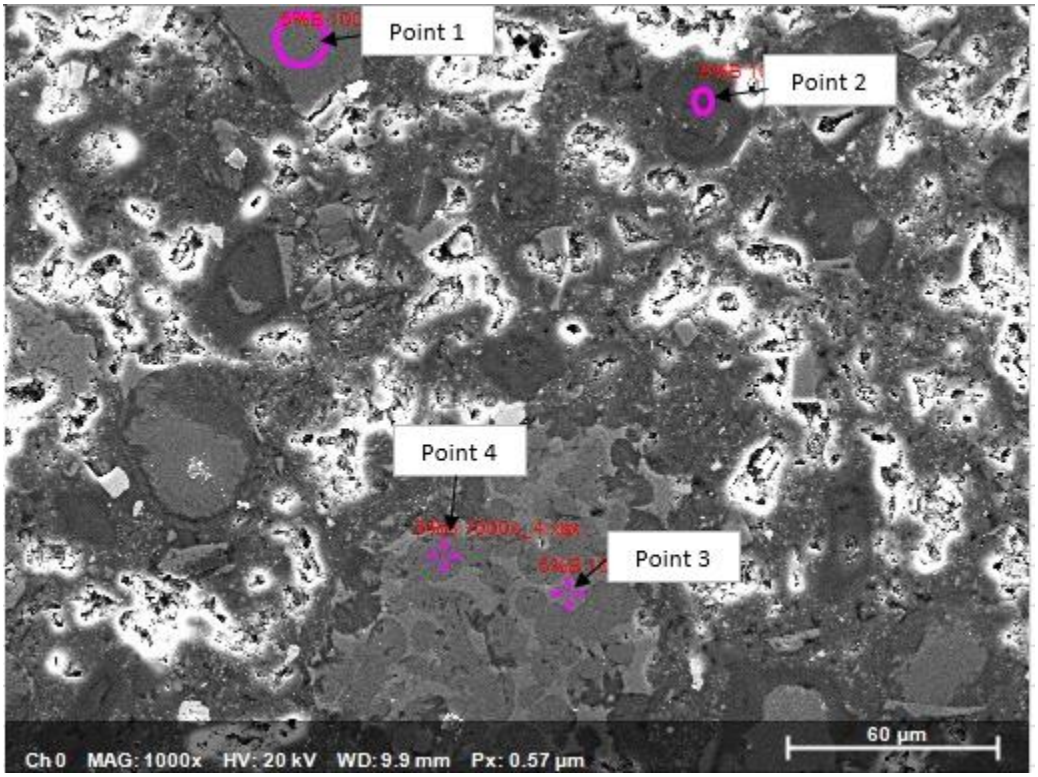


**Figure H. 4 - Points used for EDS evaluation of 5% BWOC nanoparticle barite sample.**

**Table H. 4 - EDS results for 5% BWOC nanoparticle barite sample.**

| | 5% BWOC Nanoparticle Barite Bulk Composition (%) | | | | | | | |
|---|---|---|---|---|---|---|---|---|
| | Oxygen | Sodium | Aluminum | Silicon | Sulfur | Calcium | Iron | Barium |
| Point 1 | 44.29 | 0.00 | 0.42 | 12.63 | 0.32 | 41.24 | 1.04 | 0.06 |
| Point 2 | 62.05 | 0.76 | 0.30 | 9.75 | 0.46 | 25.29 | 1.16 | 0.24 |
| Point 3 | 46.13 | 0.00 | 6.39 | 2.79 | 0.15 | 32.91 | 11.52 | 0.11 |
| Point 4 | 44.79 | 0.81 | 0.77 | 12.78 | 0.24 | 40.39 | 0.22 | 0.00 |

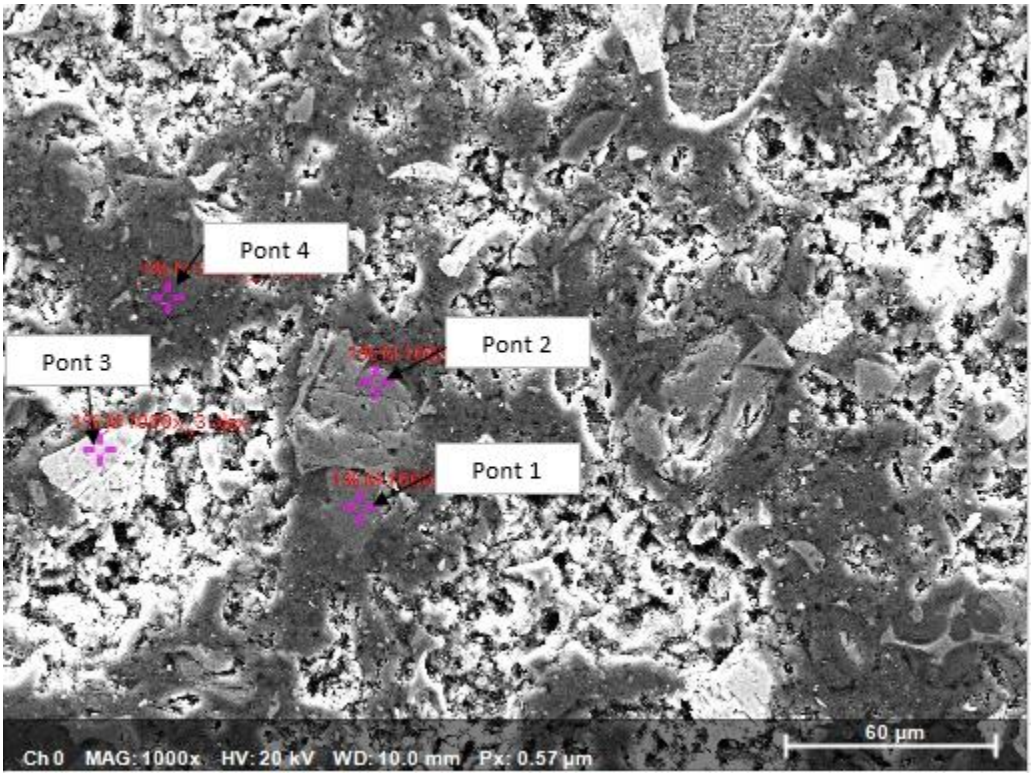


**Figure H. 5 - Points used for EDS evaluation of 1% BWOC nanoparticle magnetite sample.**

**Table H. 5 - EDS results for 1% BWOC nanoparticle magnetite sample.**

| | 1% BWOC Nanoparticle Magnetite Bulk Composition (%) | | | | | | | |
|---|---|---|---|---|---|---|---|---|
| | Oxygen | Sodium | Aluminum | Silicon | Sulfur | Calcium | Iron | Barium |
| Point 1 | 45.91 | 0.00 | 1.05 | 13.08 | 0.30 | 38.75 | 0.75 | 0.17 |
| Point 2 | 50.69 | 0.00 | 0.45 | 8.30 | 0.03 | 39.87 | 0.58 | 0.09 |
| Point 3 | 58.57 | 1.96 | 0.00 | 0.00 | 19.21 | 0.30 | 0.00 | 19.96 |
| Point 4 | 60.50 | 0.05 | 1.38 | 8.91 | 0.55 | 27.06 | 1.48 | 0.07 |

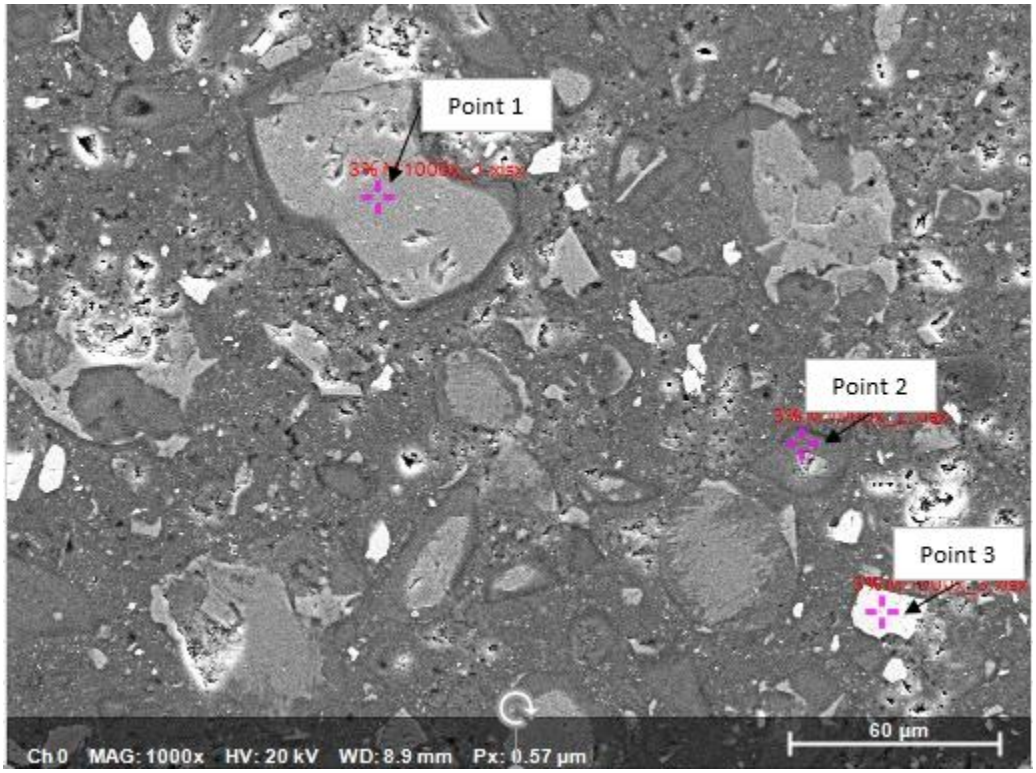


**Figure H. 6 - Points used for EDS evaluation of 3% BWOC nanoparticle magnetite sample.**

**Table H. 6 - EDS results for 3% BWOC nanoparticle magnetite sample.**

| | 3% BWOC Nanoparticle Magnetite Bulk Composition (%) | | | | | | | |
|---|---|---|---|---|---|---|---|---|
| | Oxygen | Sodium | Aluminum | Silicon | Sulfur | Calcium | Iron | Barium |
| Point 1 | 45.07 | 0.00 | 0.50 | 9.59 | 0.22 | 42.16 | 1.74 | 0.72 |
| Point 2 | 59.79 | 0.00 | 0.50 | 9.47 | 0.70 | 28.74 | 0.26 | 0.55 |
| Point 3 | 51.49 | 0.00 | 0.72 | 0.69 | 23.24 | 1.42 | 0.13 | 22.31 |

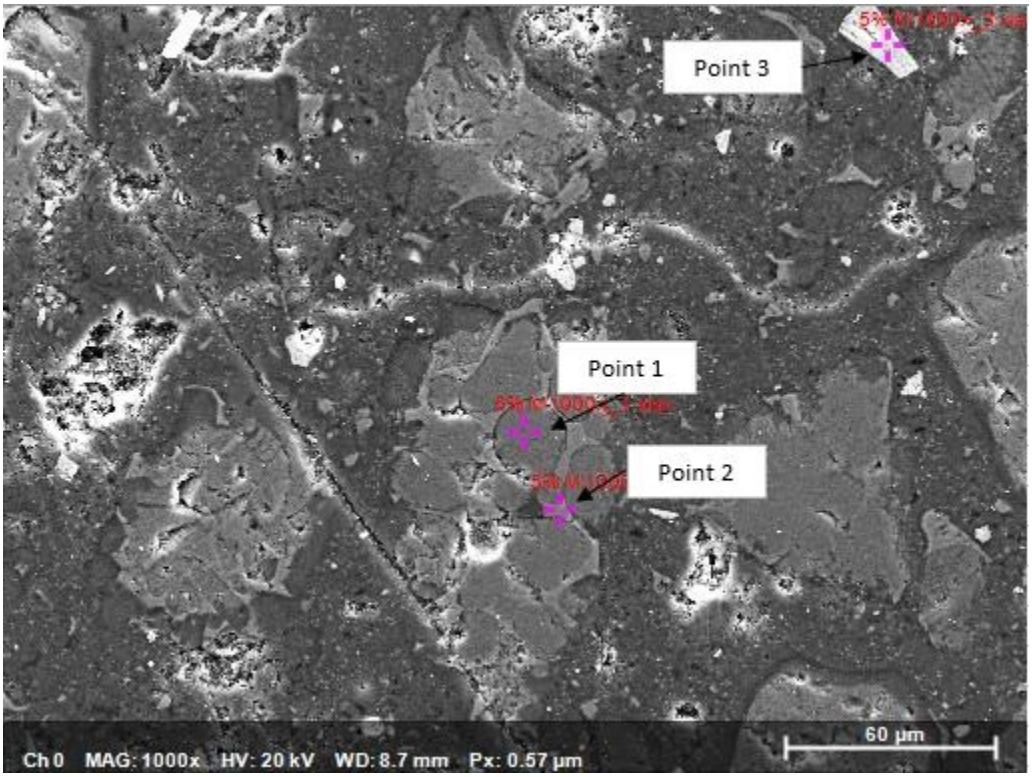


**Figure H. 7 - Points used for EDS evaluation of 5% BWOC nanoparticle magnetite sample.**

**Table H. 7 - EDS results for 5% BWOC nanoparticle magnetite sample.**

| | 5% BWOC Nanoparticle Magnetite Bulk Composition (%) | | | | | | | |
|---|---|---|---|---|---|---|---|---|
| | Oxygen | Sodium | Aluminum | Silicon | Sulfur | Calcium | Iron | Barium |
| Point 1 | 49.42 | 0.00 | 0.45 | 12.57 | 0.17 | 36.65 | 0.60 | 0.12 |
| Point 2 | 57.68 | 0.00 | 5.76 | 1.77 | 0.35 | 27.54 | 16.05 | 0.84 |
| Point 3 | 54.20 | 0.00 | 0.18 | 0.50 | 23.71 | 1.25 | 0.00 | 20.16 |

VITA

Mark Colten Ritchie

Candidate for the Degree of

Master of Science

Thesis: LABORATORY EVALUATIONS ON THE MECHANICAL IMPACT OF NANOPARTICLE ADDITIVES IN A HEAVY WELLBORE CEMENT

Major Field: Petroleum Engineering

Biographical:

Education:

Completed the requirements for the Master of Science in Petroleum Engineering at Oklahoma State University, Stillwater, Oklahoma in December 2019.

Completed the requirements for the Bachelor of Science in Mechanical Engineering at Oklahoma State University, Stillwater, Oklahoma in 2018.

Experience:

Stack Test Engineering Intern at Air Hygiene Inc., May 2017 – Aug. 2017.

Production Engineering Intern at Silverback Exploration, May. 2015 – Aug. 2016.

Engineering Intern at Priority Energy Services, May 2014 – Aug. 2014.